國立臺灣大學工學院材料科學與工程學系暨研究所

碩士論文

Department of Materials Science and Engineering

College of Engineering

National Taiwan University

Master's Thesis

# 具平面內單軸各向異性之楔形鈷鐵硼特性研究

# Study on the Characteristics of Wedge-Shaped CoFeB with In-Plane Uniaxial Anisotropy

洪翊文

Yi-Wen Hung

指導教授：白奇峰 博士

Advisor: Chi-Feng Pai, Ph.D.

中華民國 114 年 6 月

June, 2025

doi:10.6342/NTU202501047

# 國立臺灣大學碩士學位論文
# 口試委員會審定書
## MASTER'S THESIS ACCEPTANCE CERTIFICATE
## NATIONAL TAIWAN UNIVERSITY

（論文中文題目）
(Chinese title of Master's Thesisn)　具平面內單軸各向異性之楔形鈷鐵硼特性研究

（論文英文題目）
(English title of Master's Thesis)　Study on the Characteristics of Wedge-Shaped CoFeB with In-Plane Uniaxial Anisotropy

本論文係 **洪翊文** (R12527055) 在國立臺灣大學材料科學與工程學系、所完成之碩士學位論文，於民國 114 年 5 月 27 日承下列考試委員審查通過及口試及格，特此證明。

The undersigned, appointed by the Department / Graduate Institute of Material Science and Engineering on 27th/May/2025 have examined a Master's Thesis entitled above presented by **Hung, Yi-Wen** (R12527055) candidate and hereby certify that it is worthy of acceptance.

口試委員
Oral examination committee:

白奇峰 白奇峰
（指導教授 Advisor）

黃斯衍 黃斯衍

胡宸瑜 胡宸瑜

系（所、學位學程）主管 Director：蔡豐羽 蔡豐羽

doi:10.6342/NTU202501047

# 致謝

首先要先謝謝白老師，這兩年的期間總是給我的研究許多建議與方向，才使得我能夠順利完成研究，也很感謝黃斯衍老師願意借用機台以及研究助理:冠舟的協助，才能讓我順利完成 FMR 以及 VSM 的量測。

接下來我想先感謝宇豪學長和唯邦學長，感謝他們在我剛進實驗室時帶我進行實驗室儀器的訓練，為我之後的實驗奠定了良好的基礎。接著我想感謝文翰學長和沛汝學姐，感謝他們帶我做黃光製程，教會了我如何將從奈米機電中心學到的儀器應用在自己的實驗中，也提供了一些在做黃光製程的小技巧。再來要感謝瑞旭學長和胤鈞學長，感謝他們給了我不少協助，也在我實驗遇到問題時提供建議與解答，有時也能一起討論遇到的問題，多虧了他們才讓我得實驗能夠繼續執行下去。當然也感謝同屆的同學，詠絢、書鋒、智晨、冠宇，謝謝他們在實驗時的時間裡一起互相交換重要資訊，在修課時互相幫助，遇到困難時也會互相關心，有他們的陪伴讓我在實驗室的生活不會覺得孤單。也要感謝後來加入實驗室的學弟妹們，有他們的加入讓我們忙碌的實驗生活增添了一點色彩。

最後我想感謝我的家人們，有他們的支持讓我能夠無後顧之憂的完成學位。



doi:10.6342/NTU202501047

# 中文摘要

近年來，自旋電子學（Spintronics）技術在自旋軌道矩（Spin-Orbit Torque, SOT）與磁性異質結構的研究上引起廣泛關注，其中單軸各向異性（Uniaxial Anisotropy）對磁性薄膜的磁化動力學影響更是核心議題之一。本研究的動機在於探索如何透過楔形沉積（Wedge Deposition）調控 CoFeB/Pt 結構中的單軸各向異性，並進一步分析其對磁性行為與動態特性的影響，這對於提升自旋電子學元件的性能與穩定性至關重要。

本研究製備了兩個系列的 CoFeB/Pt 樣品，皆透過磁控濺鍍機進行鍍膜，其中一組為均勻（Uniform）薄膜，另一組則透過楔形沉積使得鐵磁層（CoFeB 層）具有單軸各向異性，並調控楔形沉積與基板 x 軸的夾角範圍從 0 至 180 度，每 30 度為一個單位。透過雷射磁光克爾效應（Laser-MOKE）與振動樣品磁力儀（VSM）量測，我們確認了具有楔形結構的樣品之易磁軸（Easy Axis）與楔形方向一致。

隨後，我們利用自旋轉移力矩鐵磁共振（ST-FMR）進行頻率掃描，透過 Kittel 公式擬合獲得所有樣品的去磁場（Demagnetization Field，即 $4\pi M_{eff}$），並藉由共振線寬與頻率的關係進一步分析其阻尼常數（Damping Constant）。此外，透過 ST-FMR 角度掃描（Angle Scan），我們分析不同角度下的共振場變化，進一步量化單軸各向異性的大小。最後，我們對相同樣品進行鐵磁共振（FMR）量測，以比較不同量測技術的吻合程度，結果顯示兩者高度一致，驗證了本研究方法的可靠性。

本研究不僅加深了對楔形沉積 CoFeB/Pt 結構磁性行為的理解，也為磁性異質結構中單軸各向異性的調控提供了實驗依據，對於自旋電子學與未來高效磁性記憶體元件的開發具有重要價值。

**關鍵字：**自旋轉移力矩鐵磁共振、鐵磁共振、單軸各向異性、楔形沉積



doi:10.6342/NTU202501047

# Abstract

In recent years, spintronics has garnered significant attention, particularly in the study of spin–orbit torque (SOT) and magnetic heterostructures. Among the key issues is the role of uniaxial magnetic anisotropy in influencing the magnetization dynamics of ferromagnetic thin films. This study aims to explore how uniaxial anisotropy in CoFeB/Pt structures can be engineered via wedge deposition, and to analyze its impact on magnetic behavior and dynamic properties—an essential step toward improving the performance and stability of spintronic devices.

Two series of CoFeB/Pt samples were fabricated via magnetron sputtering: one with uniform CoFeB thickness and the other incorporating a wedge-shaped CoFeB layer to introduce uniaxial anisotropy. The deposition angle relative to the substrate x-axis was varied from 0° to 180° in 30° steps. Magneto-optical Kerr effect (MOKE) and vibrating sample magnetometry (VSM) measurements confirmed that the easy axis of the wedge-deposited samples aligned with the wedge direction.

Subsequently, spin-torque ferromagnetic resonance (ST-FMR) frequency scans were conducted to extract the demagnetization field ($4\pi M_{eff}$) via Kittel fitting. In addition, the damping constant was obtained by analyzing the frequency dependence of the linewidth. Angular-dependent ST-FMR measurements were also performed to



doi:10.6342/NTU202501047

analyze how the resonance field varies with magnetic field direction, enabling quantitative evaluation of the uniaxial anisotropy strength.

To further verify the consistency of the results, ferromagnetic resonance (FMR) measurements were conducted on the same set of samples. The comparison between the two techniques demonstrated strong agreement in terms of trends and extracted parameters, confirming the reliability of the experimental methods.

This study not only deepens the understanding of magnetic behavior in wedge-deposited CoFeB/Pt structures but also provides a practical foundation for tuning uniaxial anisotropy in magnetic heterostructures. The findings have significant implications for the development of next-generation spintronic devices and high-efficiency magnetic memory technologies.

**Keywords:** spin-torque ferromagnetic resonance, ferromagnetic resonance, uniaxial anisotropy, wedge deposition



doi:10.6342/NTU202501047

# Contects





doi:10.6342/NTU202501047

doi:10.6342/NTU202501047

# List of Figures





doi:10.6342/NTU202501047

doi:10.6342/NTU202501047

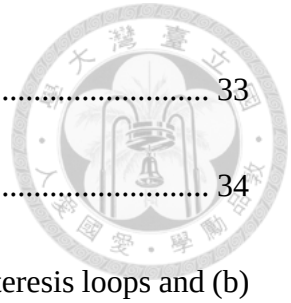





doi:10.6342/NTU202501047

doi:10.6342/NTU202501047

doi:10.6342/NTU202501047

# List of Tables





doi:10.6342/NTU202501047

# I. Introduction

## 1-1 Magnetic Anisotropy

Magnetic anisotropy describes the directional preference in a material's magnetic characteristics, influencing the energy required for magnetization. This inherent property is fundamental in shaping the magnetic behavior of materials, influencing their domain structure, coercivity, and stability. The presence of anisotropy in a material leads to preferential directions for magnetization, significantly affecting how a material responds to external magnetic fields and its performance in applications like data storage[1-3], sensors[4], and spintronic oscillators[5].

Magnetic anisotropy arises from various intrinsic and extrinsic factors, including crystallographic structure[6, 7], sample geometry[8, 9], internal stresses[10-12], and external magnetic or electric fields[13-16], all of which dictate the preferred magnetization directions and influence a material's overall magnetic response. By adjusting these factors through strain engineering, interface modification, or external field tuning, magnetic anisotropy can be precisely controlled to optimize material performance for specific applications.



doi:10.6342/NTU202501047

While magnetic anisotropy can arise from various sources, two key factors that strongly influence magnetization behavior are Shape Anisotropy, which originates from the sample's geometry, and Uniaxial Anisotropy, which describes a material's tendency to favor magnetization along a specific axis. These aspects will be discussed in the following sections.

## 1-1.1 Shape Anisotropy

Shape anisotropy plays a crucial role in determining a material’s magnetization behavior. This form of anisotropy arises purely from the geometry of a material, where the distribution of magnetic dipoles and demagnetizing fields leads to preferred magnetization directions.

In ferromagnetic materials, shape anisotropy is particularly significant when the sample is not spherical. For example, in a ferromagnetic rod with elongated geometry, as shown in **Figure1. 1**[3], the long axis often becomes the easy axis of magnetization due to the minimization of magnetostatic energy. Conversely, magnetization along the shorter axis is energetically unfavorable, defining it as the hard axis.



doi:10.6342/NTU202501047

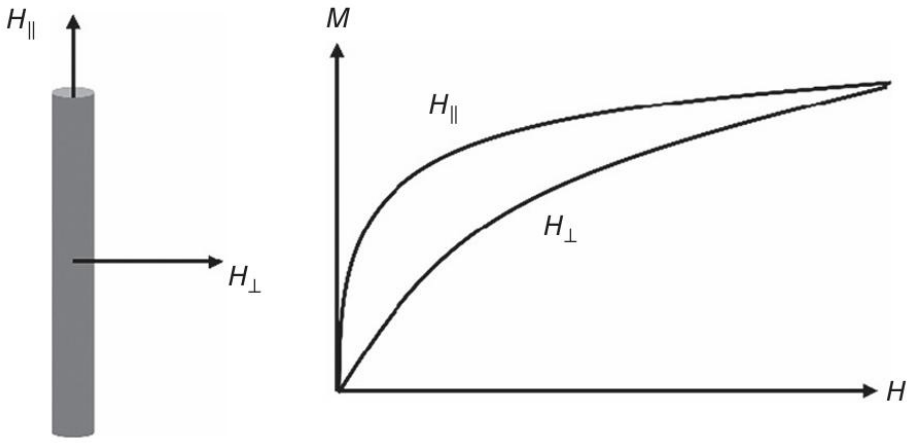


**Figure1. 1** Illustration of shape anisotropy in a ferromagnetic rod: (left) schematic showing the easy (long) and hard (short) axes due to the rod's elongated geometry; (right) corresponding M–H curves measured along the easy and hard axes.[3]

This phenomenon is a direct consequence of the demagnetizing field, which is the internal field generated by the sample's own magnetization, and its magnitude can be described as $H_{demag} = -\boldsymbol{N}M_s$, where the $\boldsymbol{N}$ is the demagnetization factor, which varies with the sample shape[17, 18] and $M_s$ is the saturation magnetization of the material. A larger demagnetization field opposes magnetization in certain directions, making it more difficult to sustain magnetization along those axes. As a result, shape anisotropy plays a critical role in designing magnetic storage devices, magnetic sensors, and spintronic applications, where controlled magnetization behavior is essential.



doi:10.6342/NTU202501047

## 1-1.2 Uniaxial Anisotropy

Uniaxial anisotropy is characterized by a material's preference for magnetization along a specific axis, known as the easy axis. Magnetization can align in either of two opposite directions (separated by 180°) along this axis, minimizing the system's energy. Alignment along the hard axis, which is typically perpendicular to the easy axis, requires overcoming higher energy states, making it more difficult for the magnetization to align in this direction, as shown in the following **Figure1. 2**[3].

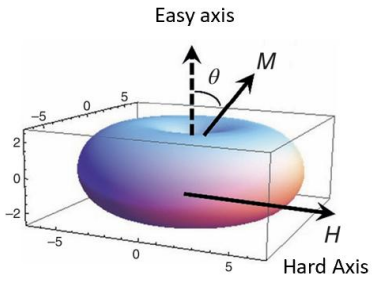


**Figure1. 2** Visualization of uniaxial anisotropy energy density for in-plane case[3]

As discussed earlier, uniaxial anisotropy can be quantified from an energy perspective, where the energy difference between the easy axis and hard axis defines the anisotropy strength. Alternatively, uniaxial anisotropy can also be characterized through the anisotropy field, which will be discussed in the following section.

Uniaxial anisotropy plays a crucial role in several technologies, particularly in magnetic memory devices like hard disk drives (HDD)[19] and magnetic random-access



doi:10.6342/NTU202501047

memory (MRAM)[20, 21], where the precise control of magnetization directions directly influences data storage and retrieval. The strength of uniaxial anisotropy in these applications determines the stability of the magnetization, which is essential for ensuring reliable data retention over time. In HDDs, for example, having a clearly defined uniaxial anisotropy helps maintain stable magnetization along the easy axis, reducing the risk of data corruption caused by thermal fluctuations. In MRAM, where fast and reliable switching between magnetic states is essential, precise control over the anisotropy enables quick response times without sacrificing data stability.

However, stronger anisotropy is not always better. Excessively strong anisotropy can make it difficult to switch magnetization directions, restricting the functionality of devices that rely on magnetization switching. On the other hand, insufficient anisotropy may lead to unstable magnetization, reducing the reliability and performance of the device. Thus, optimizing the strength and stability of uniaxial anisotropy is essential to achieve the desired functionality in these advanced technologies.



doi:10.6342/NTU202501047

## 1-1.3 Anisotropy Field

Anisotropy field ($H_k$) is also a crucial parameter that quantifies the strength of magnetic anisotropy in a material, which can be directly measured in experiments. It represents the external magnetic field required to align magnetization along the hard axis, overcoming the material's intrinsic anisotropy energy barrier. For uniaxial anisotropy, $H_k$ is related to the anisotropy energy density $K$ and the saturation magnetization $M_s$ by the expression:$H_k = \frac{2K}{\mu_0 M_s}$ [22, 23] where $\mu_0$ is the permeability of free space. This field provides an experimentally measurable way to characterize magnetic anisotropy, complementing the energy-based theoretical definition discussed in the previous section.

The anisotropy field ($H_k$) can be determined using several experimental techniques, including Vibrating Sample Magnetometry (VSM)[24], Magneto-Optical Kerr Effect (MOKE)[23, 25], and Ferromagnetic Resonance (FMR)[26]. These methods allow for the precise measurement of magnetization behavior and the identification of the field corresponding to the anisotropy strength, providing valuable insights into the material's magnetic properties.



doi:10.6342/NTU202501047

# 1-2 Wedge Deposition

Wedge deposition is a technique that creates a thin film with a controlled thickness gradient across the substrate, resulting in a wedge-shaped profile. This method is achieved by oblique angle deposition, where the substrate is tilted relative to the material flux[27-30], or using a shadow mask[31, 32], causing the thickness of the film to gradually change from one side of the substrate to the other. By inducing this thickness gradient, it becomes possible to manipulate factors such as strain, interface effects, and dipolar interactions[33-35], which can significantly influence material properties like anisotropy, coercivity, and resistivity. In particular, wedge deposition is an effective tool for inducing or enhancing uniaxial anisotropy[28, 36, 37], making it highly valuable for the study and optimization of thin film magnetism.

In this work, wedge deposition is achieved through oblique angle deposition, where the substrate is tilted relative to the material flux, creating a gradual thickness gradient. This method introduces directional strain and modifies the atomic arrangement, causing a preferential alignment of magnetic domains. The oblique deposition angle influences the shadowing effect and enhances the development of uniaxial anisotropy, as atoms tend to accumulate more densely along one direction, promoting strong directional properties in the resulting thin films. By precisely controlling the deposition angle and the thickness



doi:10.6342/NTU202501047

gradient, we were able to create a CoFeB layer with enhanced uniaxial anisotropy, crucial for optimizing the magnetic performance of the material.

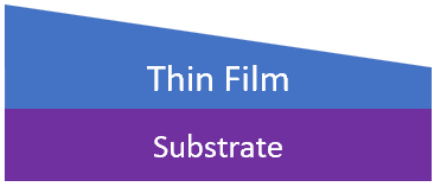


**Figure1. 3** Schematic of a wedged-shape sample prepared by wedge deposition, illustrating the gradual thickness variation along the wedge direction.

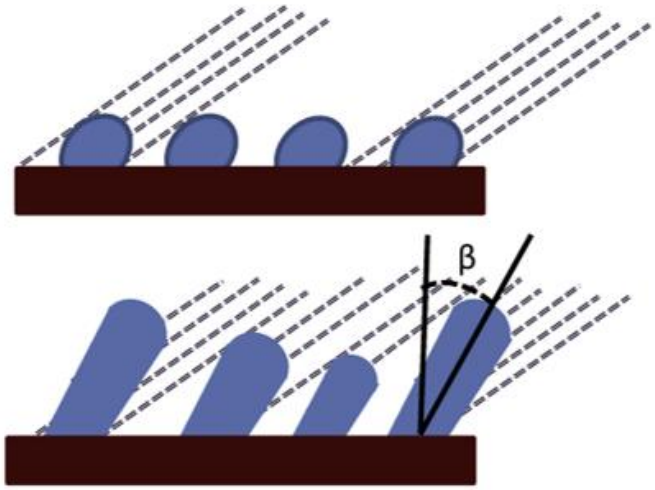


**Figure1. 4** Schematic of the oblique angle deposition, where material is deposited onto the substrate at a tilted incident angle[27]



doi:10.6342/NTU202501047

# 1-3 Ferromagnetic Resonance(FMR)

## 1-3.1 History of FMR

Ferromagnetic Resonance (FMR) was first introduced by Charles Kittel in 1948 as a fundamental method for studying the dynamic behavior of magnetization in ferromagnetic materials. Kittel's work[38] established the theoretical framework for FMR, describing how the precession of magnetization around the effective field could be excited by an external microwave frequency. This discovery provided a crucial tool for investigating intrinsic magnetic properties, such as gyromagnetic ratios, damping mechanisms, and magnetic anisotropy.

Early experimental observations of FMR were conducted using electron spin resonance (ESR) techniques[39, 40], where a microwave field was applied to a ferromagnetic sample under an external magnetic field. By measuring the absorption spectrum, researchers identified a resonance condition when the microwave frequency matched the natural precessional frequency of magnetization. These studies primarily focused on bulk ferromagnetic materials, such as iron, nickel, and cobalt, laying the foundation for understanding magnetic relaxation processes and spin dynamics. As research progressed, the focus gradually shifted from ESR setups to more dedicated FMR



doi:10.6342/NTU202501047

systems, which offered improved sensitivity, better frequency control, and broader applicability—particularly in thin films and nanostructures. This transition helped establish FMR as a powerful and widely adopted tool for exploring spin dynamics, magnetic anisotropy, and damping in modern magnetic materials.

## 1-3.2 Different Types of FMR

Ferromagnetic Resonance (FMR) has evolved through various measurement techniques, each tailored to specific research needs and material systems. The earliest and most traditional method is Cavity-based FMR[41, 42], which employs a microwave resonant cavity to generate a uniform RF magnetic field around the sample. The sample is placed within the cavity, and its resonance is detected by measuring changes in cavity quality factor (Q-factor) or microwave absorption, as shown in **Figure1. 5**. This method provides high sensitivity and precise linewidth measurements, making it particularly useful for bulk materials, single crystals, and insulating magnetic materials. However, Cavity-based FMR has limitations, including its fixed resonance frequency and relatively large setup, which restricts flexibility in exploring frequency-dependent properties.

To overcome these limitations and adapt to modern thin-film and spintronics research, Chip-based FMR[43-47], utilizing coplanar waveguides (CPW) or microstrip



doi:10.6342/NTU202501047

lines, has been widely adopted. This approach allows for broadband frequency measurements by directly applying an RF signal from a Vector Network Analyzer (VNA) or a signal generator. A schematic of a typical setup is shown in **Figure1. 6**. Compared to cavity-based methods, chip-based FMR offers greater flexibility, as it does not require a fixed resonant structure and can be easily integrated with other experimental setups. Additionally, it helps the study of thin films, nanostructures, and patterned magnetic devices, where sample size and geometry play a crucial role. The use of lock-in amplifiers and advanced detection techniques further enhances measurement sensitivity, making chip-based FMR an essential tool in modern magnetism and spintronics research.

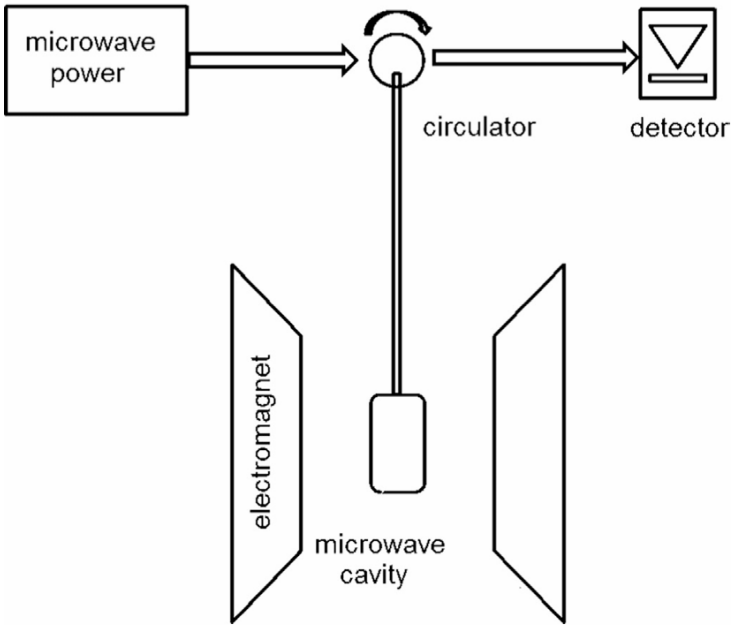


**Figure1. 5** Experimental setup of a cavity-based FMR measurement.[44]



doi:10.6342/NTU202501047

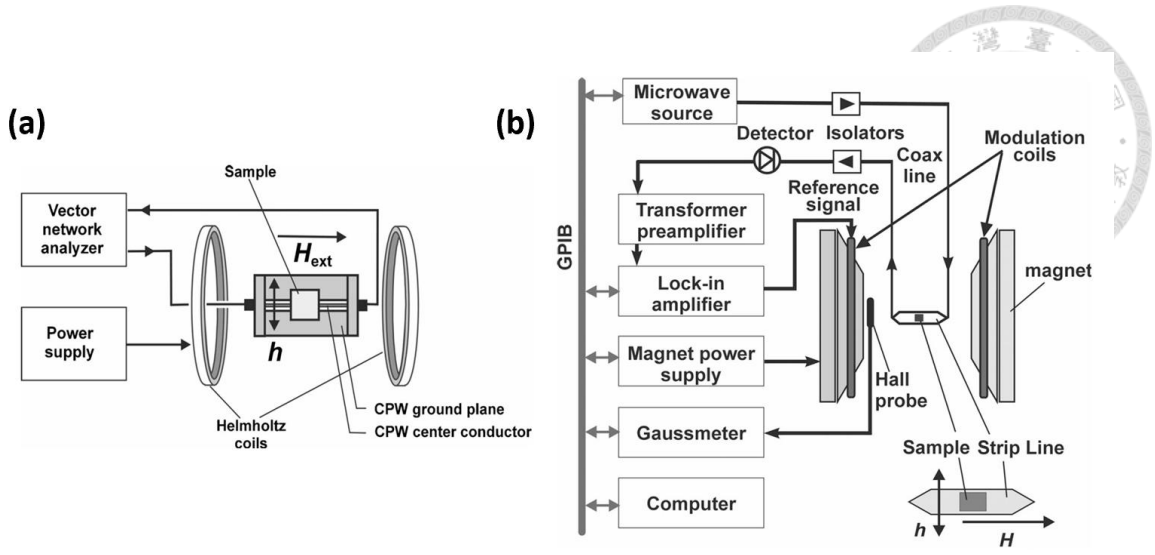


**Figure1. 6** Schematic diagrams of (a) chip-based VNA-FMR and (b) stripline FMR setups. [43]

## 1-3.3 Spin-Torque Ferromagnetic Resonance(ST-FMR)

Spin-Torque Ferromagnetic Resonance (ST-FMR)[48-50] is a versatile technique for probing magnetization dynamics using spin currents instead of external RF magnetic fields. Unlike conventional FMR, which excites magnetization via an oscillating field, ST-FMR relies on a microwave-frequency charge current that generates a spin current through spin-transfer torque (STT) [51] or spin-orbit torque (SOT) [52, 53]. Consequently, this spin current interacts with the magnetization, driving resonance in the sample. The corresponding measurement setup is illustrated in **Figure1. 7**

Furthermore, the precessing magnetization modulates resistance via anisotropic magnetoresistance (AMR)[54, 55], spin Hall magnetoresistance (SMR)[56, 57], or giant



doi:10.6342/NTU202501047

magnetoresistance (GMR)[58, 59]. This resistance oscillation, mixed with the microwave current, yields a detectable DC voltage. Analyzing this voltage as a function of field and frequency allows extraction of key parameters such as damping, anisotropy, and torque efficiency.

Compared to conventional FMR, ST-FMR is especially useful for studying spintronic effects in heavy metal/ferromagnet heterostructures. It enables direct quantification of spin-torque efficiency, playing a vital role in the optimization of spintronic devices, including MRAM, logic circuits, and RF nano-oscillators.

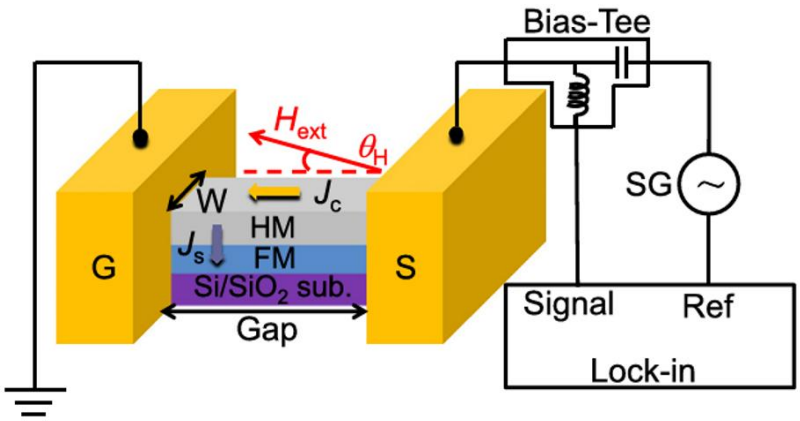


**Figure1. 7** Schematic of an ST-FMR measurement setup using a lock-in amplifier and bias tee. [50]



doi:10.6342/NTU202501047

# 1-4 Theory of FMR

## 1-4.1 Landau-Lifshitz-Gilbert(LLG) Equation

The Landau-Lifshitz-Gilbert (LLG) equation is a fundamental equation describing the dynamics of magnetization in a ferromagnetic system. It governs how the magnetization vector $\boldsymbol{M}$ evolves over time in response to an effective magnetic field $\boldsymbol{H}_{\mathbf{eff}}$, as shown in **Figure1. 8**, incorporating both precessional motion(second term) and damping effects(first term). The LLG equation is expressed as:

$$\frac{d\mathbf{M}}{dt} = -\gamma \mathbf{M} \times \mathbf{H}_{eff} + \frac{\alpha}{M_s} \mathbf{M} \times \frac{d\mathbf{M}}{dt} \qquad \textbf{(1. 1)}$$

where:

- $\gamma$ is the gyromagnetic ratio, determining the precession frequency of the magnetization;
- $\mathbf{H}_{eff}$ is the effective magnetic field, including external, demagnetizing, and anisotropy contributions;
- $\alpha$ is the Gilbert damping parameter, describing the relaxation rate of the magnetization toward equilibrium;
- $M_s$ is the saturation magnetization.



doi:10.6342/NTU202501047

The LLG equation forms the foundation for understanding ferromagnetic resonance (FMR). When an oscillating external field is applied perpendicular to the equilibrium magnetization, it induces precessional motion, which can be experimentally observed as FMR. The resonance condition and linewidth of the FMR signal are directly influenced by the parameters in the LLG equation, particularly the damping coefficient $\alpha$.

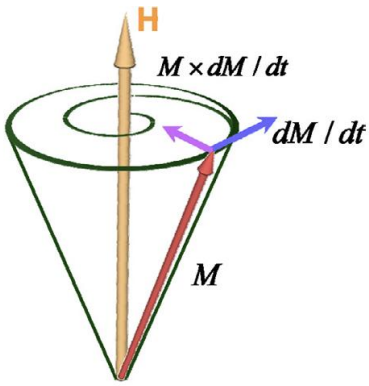


**Figure1. 8** Dynamics of magnetization precession with damping. [60]

## 1-4.2 Kittel Formula

The Kittel formula describes the resonance condition for FMR by relating the resonance frequency $f$ to the applied magnetic field $H$. It provides a key theoretical framework for interpreting experimental FMR spectra. The general form of the Kittel equation for a thin film with in-plane magnetization is:

$$f = \frac{\gamma}{2\pi}\sqrt{(H + H_k)(H + H_k + 4\pi M_{eff})} \qquad \textbf{(1. 2)}$$



doi:10.6342/NTU202501047

Where:

- $H$ is the externally applied magnetic field;
- $H_k$ represents the uniaxial anisotropy field, $4\pi M_{eff}$ is the demagnetizing field for thin films;
- $\gamma$ is the gyromagnetic ratio.

This equation shows that the resonance frequency depends not only on the applied field but also on the intrinsic magnetic properties of the material, such as saturation magnetization and anisotropy fields. Different geometries and material conditions result in variations of the Kittel formula. For instance, in an out-of-plane configuration or for bulk materials, additional terms accounting for demagnetization effects and anisotropy modifications may be included.

The Kittel equation is extensively used to extract key magnetic parameters from FMR experiments. By measuring the resonance frequency as a function of applied field, researchers can determine properties such as the gyromagnetic ratio, saturation magnetization, and anisotropy fields. This makes the equation essential for characterizing magnetic thin films and heterostructures in both fundamental research and technological applications.



doi:10.6342/NTU202501047

# II. Experiment

## 2-1 Magnetron Sputtering

Sputtering is a widely used physical vapor deposition (PVD) technique for fabricating thin films. The process involves ionizing an inert gas (typically argon) to generate plasma, which bombards the target material, ejecting atoms that then condense onto the substrate to form a film. Magnetron sputtering enhances this process by incorporating a magnetic field near the target, increasing ionization efficiency and deposition rates while reducing substrate damage.

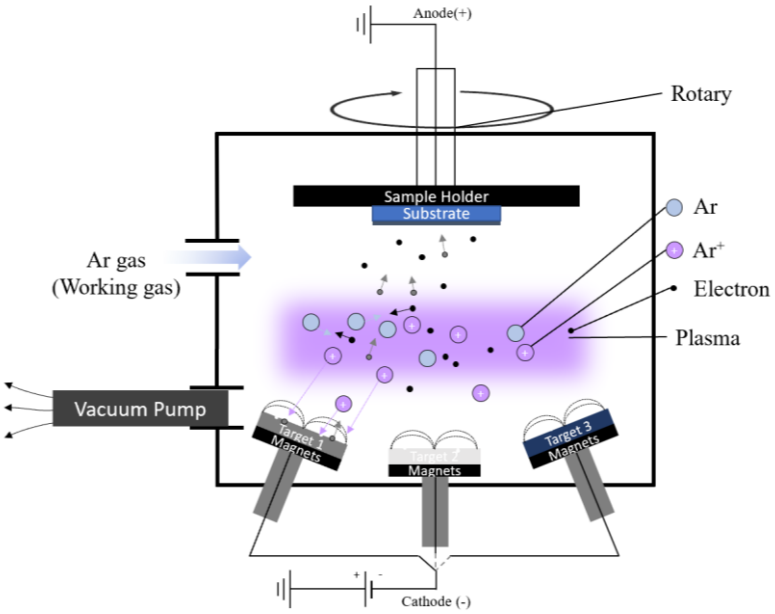


**Figure2. 1** Magnetron sputtering system schematic.

In this study, thin films were deposited on $SiO_2$ substrate by using magnetron sputtering. The substrate was rotated in 10rpm for all uniform samples, and Oblique



doi:10.6342/NTU202501047

Angle deposition is applied for wedged-shape samples (i.e. keep the substrate static). The Oblique Angle for wedge deposition is about 25 degree apart from substrate normal. The deposition conditions of different materials are summarized in the following **Table2. 1** Deposition conditions for different sputtering materials.

| Material | $Co_{20}Fe_{60}B_{20}$ | Pt | Ta |
|---|---|---|---|
| Base Pressure(Torr) | 5E-7 | | |
| Working Gas | Ar | | |
| Working Pressure(mTorr) | 1.5 | 3 | 3 |
| Power(W) | 90 | 30 | 30 |
| Growth Rate (s/nm) | 24 | 23 | 35.6 |
| Growth Rate (nm/s) | 0.0416 | 0.0435 | 0.0281 |

**Table2. 1** Deposition conditions for different sputtering materials.

# 2-2 ST-FMR Device Fabrication

## 2-2.1 Sample Structure

To fabricate an ST-FMR device, a ferromagnetic layer and a heavy metal layer are required. The heavy metal layer enables the Spin Hall effect[61, 62], which generates spin-orbit torque (SOT) to drive the ferromagnetic resonance. In this study, a CoFeB/Pt/Ta multilayer structure is used, where CoFeB serves as the ferromagnetic layer, and Pt acts as the primary spin source due to its strong Spin Hall effect. While Ta also contributes to the Spin Hall effect, its main role is as a capping layer.



doi:10.6342/NTU202501047

This work investigates two series of samples: one with a uniform CoFeB layer, which turning the rotary on, varying its thickness from 2 nm to 10 nm in 2 nm increments, and another exploring different wedge deposition angles relative to the x-axis. The wedge angle is varied from 0° to 180° in 30° steps. For the wedge-deposited series, the nominal thicknesses are defined as 6 nm and 8 nm based on the deposition time, representing the average thickness near the center of the substrate.

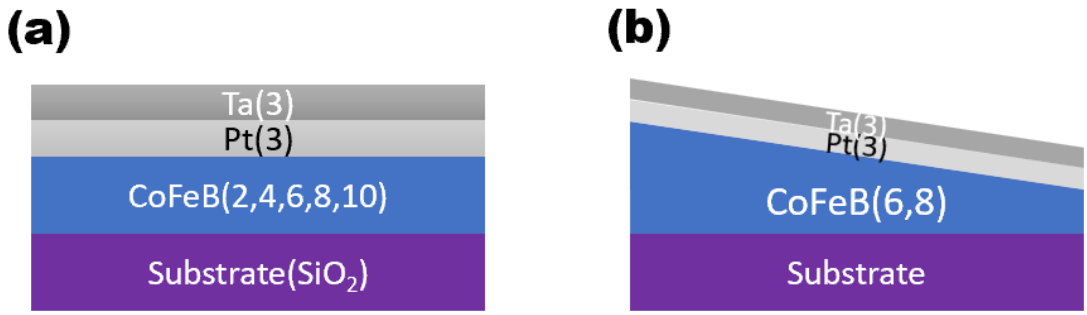


**Figure2. 2** Structure schematics of (a) uniform samples and (b) wedge-shaped samples used in this study.

## 2-2.2 Photolithography

Photolithography is a key technique for defining precise micro- and nanoscale patterns in thin film devices. It works by coating the sample with a light-sensitive photoresist, then exposing it to UV light through a patterned mask. The exposed regions undergo chemical changes that allow selective removal during development. This method enables high-resolution patterning, making it essential for applications ranging from semiconductor circuits to spintronic devices.



doi:10.6342/NTU202501047

In this study, photolithography was used to define the device geometry. The process involved spin-coating a positive photoresist, UV exposure through a designed mask, and development to reveal the desired pattern, as detailed in the following:

1. **Pre-cleaning the samples:** All samples are placed in a cup of isopropyl alcohol and subjected to ultrasonic vibration for 1 minute. Afterward, an air gun is used to dry the samples.
2. **Baking before spin coating:** To remove any residual isopropyl alcohol and moisture, all samples are baked on a hot plate at 100°C for 1 minute before spin coating.
3. **Spin Coating:** A positive photoresist(PR) is dropped onto each sample. The spin coating process follows this recipe: Step 1: 3000 rpm for 10 seconds/Step 2: 4000 rpm for 30 seconds. This results in a uniform PR thin film on all samples.
4. **Soft-Baking:** The samples are baked on a hot plate at 100°C for 2 minutes to dry and solidify the PR.
5. **Aligning and exposure:** Each sample is placed into the aligner (SUSS MA/BA8 Gen3) along with a mask. The pattern is aligned on the sample, and UV light is exposed for 10 seconds to transfer the mask pattern onto the PR. This step is repeated until all samples have been exposed.



doi:10.6342/NTU202501047

6. **Development:** The exposed samples are placed in a TMAH solution and gently agitated. The exposed PR dissolves in the solution, while the unexposed regions remain intact on the sample.
7. **Check the result:** Optical microscopy (OM) is used to verify that the patterns match the expected dimensions (e.g., length, width).

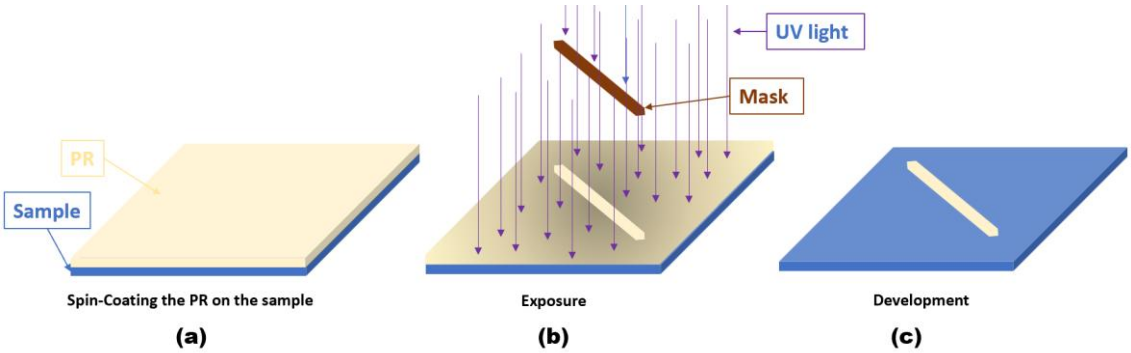


**Figure2. 3** Process flow of a positive photoresist photolithography process:

(a) spin coating, (b) exposure, and (c) development.

## 2-2.3 Ion-Beam Etching(IBE)

Ion-Beam Etching (IBE), also known as Ion Milling, is a physical dry etching technique widely used in microfabrication to achieve precise material removal. Unlike chemical etching methods, IBE relies on a directed ion beam to sputter material from the surface of a substrate. This technique provides excellent control over etching depth and profile, making it ideal for pattern transfer in thin-film device fabrication.



doi:10.6342/NTU202501047

In our process, IBE was conducted using a Kaufman-type ion gun, operating at a beam voltage of 250V and a beam current of 0.69A, under a chamber pressure below 2E-5Torr. A high-energy argon ($Ar^+$) ion beam was directed at the sample with an incidence angle of 60°, causing atomic-scale sputtering. The etching was performed for 120 seconds to ensure that the silicon layer was reached, with the sample continuously rotated at 10 RPM to improve uniformity and minimize directional etching effects.

Furthermore, to ensure precise control over etching depth and layer transitions, we also employed in situ Secondary Ion Mass Spectrometry (SIMS) monitoring throughout the process. By analyzing the composition of sputtered ions in real time, SIMS allowed for accurate detection of material interfaces, ensuring well-defined pattern transfer. The actual instrument setup is similar to the one shown in **Figure2. 4**.

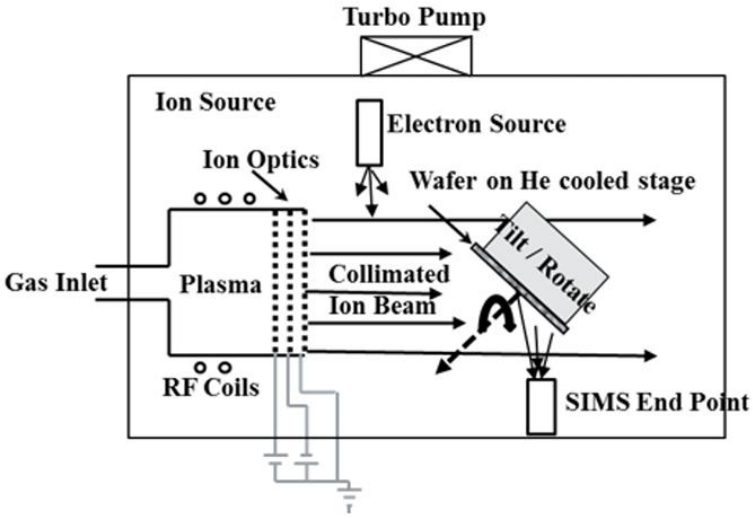


**Figure2. 4** Schematic diagram of an ion-beam etching (IBE) system. [63]



doi:10.6342/NTU202501047

## 2-2.4 Electrode deposition

The electrodes were deposited using magnetron sputtering, with deposition conditions as described in **Table2. 1**. A Ta/Pt bilayer structure was used as the electrode for the ST-FMR device. The deposition time was 2845 s for Ta and 150 s for Pt, corresponding to estimated thicknesses of approximately 80 nm and 6.5 nm, respectively. The Pt layer was included to improve the measurement signal quality when probing the device, as its high work function and surface properties facilitate better electrical contact.

## 2-2.5 Process Flow

The fabrication of the ST-FMR device follows a multi-step process, outlined as follows, with corresponding schematic diagrams provided in **Figure2. 6**:

a. **Thin Film Deposition:** The process begins with the deposition of the thin films as described in section 2-2.1 Sample Structure, forming the base material for the device.
b. **First Photolithography Step (ST-FMR Bar Definition):** After film deposition, the first photolithography process is used to define the ST-FMR bar structure. The resist is patterned to outline the desired bar shape, as illustrated in **Figure2. 5**.
c. **Etching for ST-FMR Bar:** The patterned resist is then developed, and etching is carried out to transfer the bar shape onto the film.



doi:10.6342/NTU202501047

d. **Second Photolithography Step (Electrode Patterning):** In the second photolithography step, the electrode patterns are defined on the film. A new layer of resist is applied and patterned to outline the electrode shapes, as illustrated in **Figure2. 5**.

e. **Electrode Deposition:** The Pt/Ta bilayer electrodes were deposited using magnetron sputtering, following the same conditions as previously described.

f. **Lift-off for Electrodes:** After electrode deposition, the lift-off process is used to define the electrode shapes. The resist is developed, and the unwanted metal is removed, leaving behind the Pt/Ta electrodes in the desired pattern. In this process, the sample was ultrasonically cleaned in acetone for 5 minutes, followed by isopropyl alcohol(IPA) for 30 seconds to ensure complete removal of residual resist and metal.

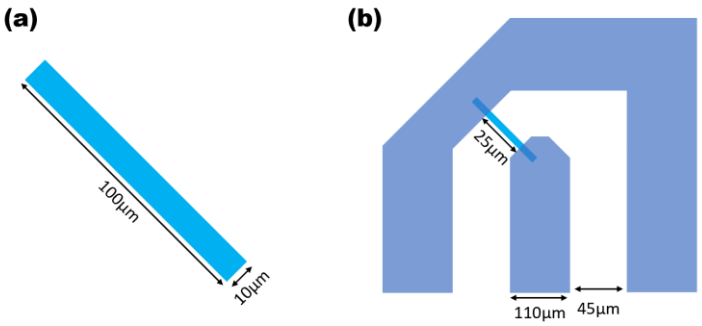


**Figure2. 5** (a) ST-FMR bar with labeled dimensions. (b) Device layout illustrating electrode shapes and contact sizes.



doi:10.6342/NTU202501047

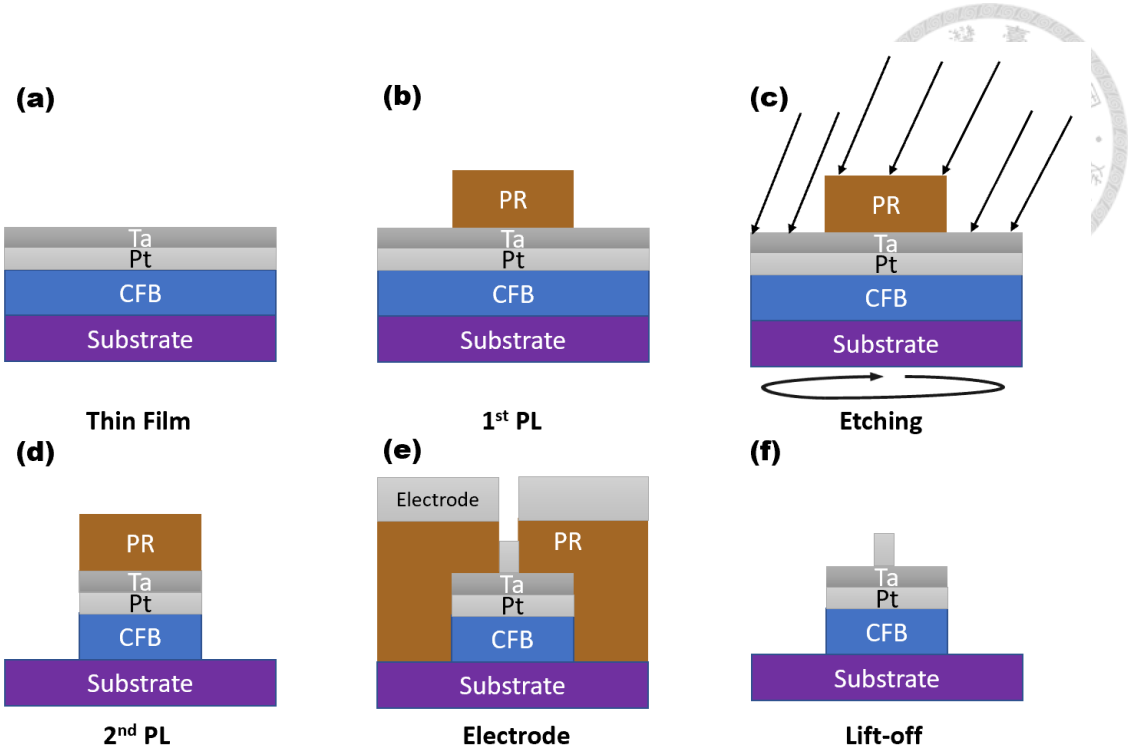


**Figure2. 6** Fabrication process flow of the ST-FMR device, including (a) thin film deposition, (b) first photolithography, (c) etching, (d) second photolithography, (e) electrode deposition, and (f) lift-off process.

Finally, the completed ST-FMR device is shown in **Figure2. 7**

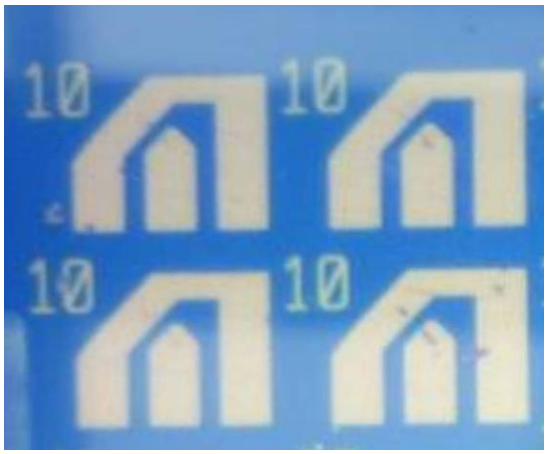

**Figure2. 7** Optical image of the final ST-FMR device after fabrication.



doi:10.6342/NTU202501047

# 2-3 Laser-MOKE

The Magneto-Optical Kerr Effect (MOKE) is a widely used technique for characterizing the magnetic properties of thin films by analyzing changes in the polarization of reflected light. When a polarized laser beam is incident on a magnetic material, the interaction between the light and the sample's magnetization induces a rotation of the polarization plane (Kerr rotation) and an intensity change (Kerr ellipticity) in the reflected beam. These magneto-optical effects provide key insights into magnetic anisotropy, coercivity, and hysteresis loop behavior. Depending on the relative orientation of the magnetization and the plane of incidence, MOKE can be categorized into longitudinal, transverse, and polar configurations, each offering different perspectives on magnetization dynamics.

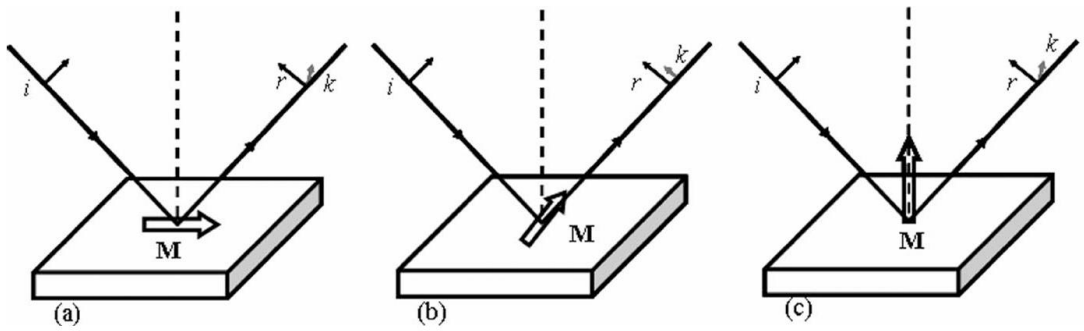


**Figure2. 8** Schematic diagrams of (a) longitudinal, (b) transverse, and (c) polar MOKE geometries.[64]

In this study, we use the longitudinal mode to measure the hysteresis loop, and a 632.8 nm He-Ne laser serves as the light source. The laser beam is initially polarized



doi:10.6342/NTU202501047

using a polarizer, ensuring that only a well-defined polarization state reaches the sample. After reflection, the beam passes through an analyzer (another polarizer) set near the extinction angle, and its intensity is detected using a photodiode.

Besides, to apply a uniform in-plane magnetic field, a pair of Helmholtz coils was placed on either side of the sample, generating a maximum field strength of 270 Oe. The coils are powered by a Lock-in Amplifier, which also supplies a low-frequency AC modulation to enhance the signal-to-noise ratio by reducing low-frequency noise. The photodiode output is fed back into the Lock-in Amplifier, enabling phase-sensitive detection and further improving measurement sensitivity.

Additionally, the sample is mounted on a motorized rotation stage, allowing for angle-dependent MOKE measurements. This enables precise characterization of the anisotropic magnetic properties as a function of the in-plane field orientation, providing deeper insights into the uniaxial anisotropy of our CoFeB films. The actual MOKE measurement system used in our experiments is shown in **Figure2. 9**.



doi:10.6342/NTU202501047

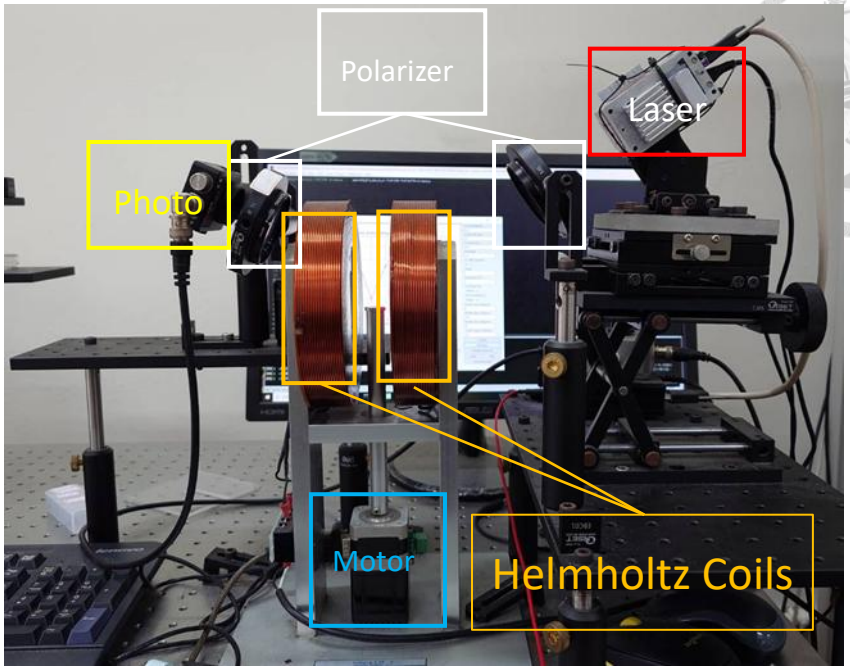


**Figure2. 9** Setup of the Laser-MOKE measurement system with labeled components.

This setup provides high-resolution, non-destructive characterization of thin-film magnetism and is particularly well-suited for analyzing uniaxial anisotropy and hysteresis loops in our deposited CoFeB films.

# 2-4 Vibrating Sample Magnetometer (VSM)

The Vibrating Sample Magnetometer (VSM) is a technique used to measure the magnetic properties of materials by detecting changes in the induced magnetic moment when a sample is vibrated within an external magnetic field. When the sample is exposed to a uniform magnetic field and vibrates mechanically, the magnetization of the sample induces a time-varying signal in nearby pickup coils. This signal is proportional to the



doi:10.6342/NTU202501047

magnetization of the sample, which can be analyzed to derive key magnetic parameters such as saturation magnetization ($M_s$), coercivity ($H_c$), and remanent magnetization($M_r$).

In a typical VSM setup, the sample is placed in a uniform magnetic field, and the sample is vibrated back and forth at a constant frequency. The resulting signal from the pickup coils is detected, and the magnetization is measured as a function of the applied field. This setup allows for the generation of hysteresis loops, which provide insight into the magnetic properties of the material, such as magnetization reversal and coercivity.

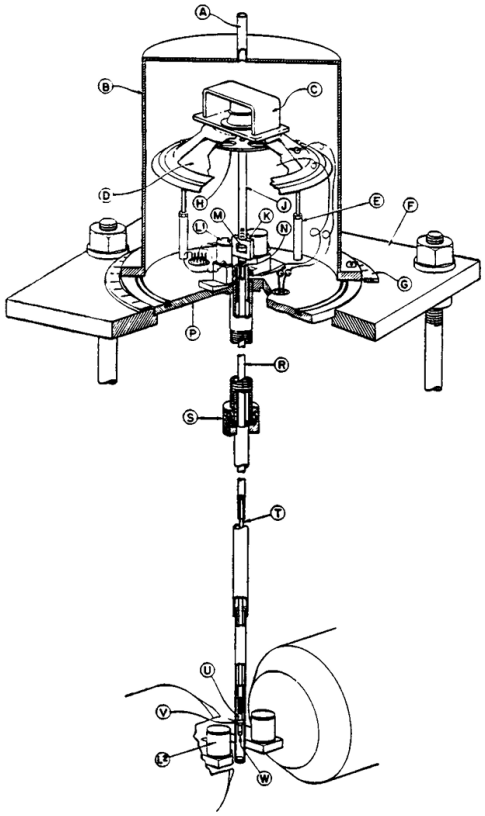


**Figure2. 10** Schematic diagram of the VSM measurement system.[65]



doi:10.6342/NTU202501047

For this study, the VSM measurements were conducted using a commercially available system equipped with an electromagnet capable of generating a variable external magnetic field, with the actual instrument setup being similar to the one shown in **Figure2. 10**. The magnetic field was swept within the range of ±8000Oe, allowing us to observe the full magnetic response of the sample, including magnetization reversal and coercivity.

In addition to standard measurements, we performed angular-dependent VSM measurements to investigate the variation in $M_r/M_s$ as the sample orientation relative to the magnetic field was varied. This helped to explore the material's magnetic anisotropy and the directional dependence of its magnetic properties.

Background signals arising from environmental or instrumental noise were removed during data processing to ensure accurate measurements. All measurements were conducted at room temperature for consistency, and multiple measurements were taken for each sample.

# 2-5 ST-FMR

In an ST-FMR experiment, an RF signal is applied through probe tips to the sample's electrodes, illustrated in **Figure2. 11**. This induces a spin current via the spin Hall effect in the heavy metal layer, causing magnetization precession. Additionally, the RF current



doi:10.6342/NTU202501047

generates a weak oscillating Oersted field that further excites the precession. When the external magnetic field satisfies the Kittel resonance condition, the resulting time-dependent magnetoresistance change (AMR or SMR) leads to a rectified DC voltage, which is measured to extract key resonance parameters.


**Figure2. 11** Illustration of the probe tips during ST-FMR measurement, with labeled Source (S) and Ground (G).

To systematically study the sample's magnetic properties, the ST-FMR experiment is conducted in two measurement series: frequency-dependent and angle-dependent measurements

**a. Frequency Dependence Measurement**

For frequency-dependent ST-FMR measurements, a sinusoidal RF signal (6–15 GHz, 20 dBm) is injected into the device through GSG-configured probe tips. After probing, the sample resistance is measured, typically ranging from 0.8 to 1.1 kΩ for a 10 μm-wide ST-FMR bar.



doi:10.6342/NTU202501047

The external magnetic field is generated using an electromagnet, sweeping from +4000 Oe to -4000 Oe. The lock-in amplifier powers the electromagnet and enhances the signal-to-noise ratio via frequency modulation at 3388 Hz, with a sensitivity setting of 50 μV and a detection range of ±150 μV.

Additionally, to investigate wedge-dependent anisotropy, measurements are performed with the wedge direction varied from 0° to 180° in 30° steps, while keeping a fixed external magnetic field.

By analyzing the frequency-dependent rectified voltage, key parameters such as the effective magnetization ($4\pi M_{eff}$) and Gilbert damping constant (α) can be extracted.

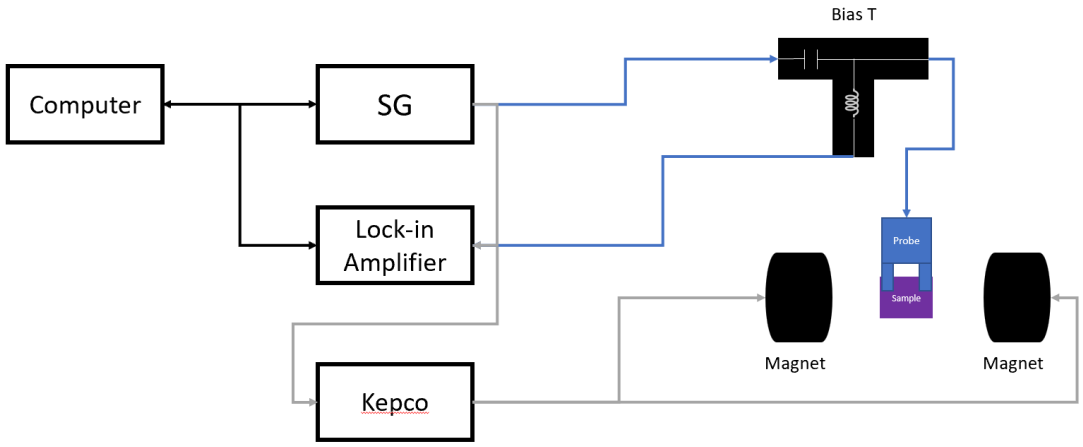


**Figure2. 12** ST-FMR measurement setup for frequency dependence.

### b. Angle Dependence Measurement

For angle-dependent measurements, the only difference from frequency-dependent measurements is the use of a GMW vector magnet instead of the electromagnet, along



doi:10.6342/NTU202501047

with a different field sweeping range and angle steps. The same modulation settings (3388 Hz) and resistance measurements (0.8 to 1.1 kΩ) are used.

The external magnetic field is varied between ±2000 Oe, with its direction swept from 0° to 360° in 10° steps. These measurements provide insight into the uniaxial anisotropy field ($H_u$) and its angular dependence.

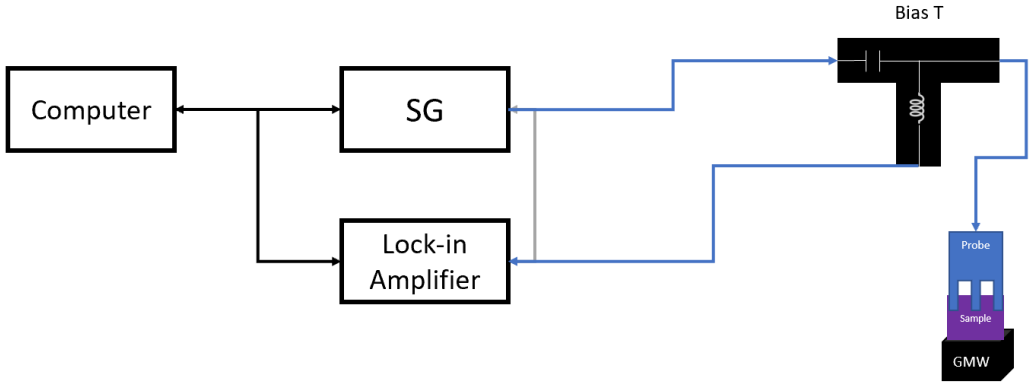


**Figure2. 13** ST-FMR measurement setup for angle dependence.

# 2-6 FMR

Ferromagnetic resonance (FMR) is a widely used technique for characterizing the dynamic properties of magnetic materials by analyzing the precessional motion of magnetization under an applied RF field. In this experiment, the FMR system consists of a coplanar waveguide (CPW) for RF excitation, field modulation for enhanced signal-to-noise ratio, and a detection setup using a lock-in amplifier. The RF magnetic field generated by the CPW is applied perpendicular to a static external field, driving the



doi:10.6342/NTU202501047

magnetization into precession. When the applied field satisfies the Kittel resonance condition, maximum energy absorption occurs.

The experiment was conducted on CoFeB thin films, including wedge-deposited CoFeB (6 nm) and uniform CoFeB (6 nm and 8 nm), all placed face-down on the waveguide to ensure direct coupling between the RF magnetic field and the thin film. The RF excitation frequency ranged from 8 to 16 GHz, while the external magnetic field was swept only within the resonance field range, with the field always applied in the positive direction and swept from higher to lower values. Besides, to investigate the angular dependence of resonance, the applied field angle was varied from 0° to 180° in 30° steps.

By analyzing the field-dependent resonance response, key magnetic parameters such as the effective magnetization ($4\pi M_{eff}$) and Gilbert damping constant (α) were extracted, providing insights into the sample's anisotropy and damping behavior.

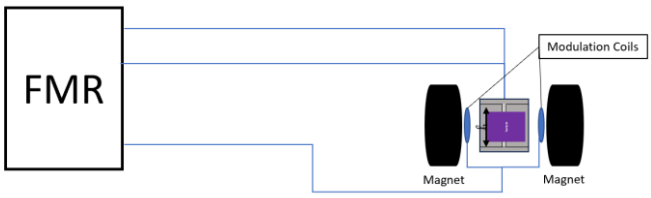


**Figure2. 14** Schematic diagram of the FMR measurement setup.



doi:10.6342/NTU202501047

# III. Results and Discussion

## 3-1 Laser-MOKE

### 3-1.1 Uniform Samples Thickness Dependence

To investigate the thickness dependence of magnetic properties, we performed Laser-MOKE measurements on uniform CoFeB samples with varying thicknesses. The MOKE hysteresis loops and the extracted coercivity ($H_c$) as a function of CoFeB thickness(**Figure 3. 1**) reveal a clear trend: $H_c$ increases with thickness, reaching a maximum at 8 nm, before slightly decreasing at 10 nm This behavior is consistent with previous studies[66]. Additionally, the MOKE signal intensity grows with increasing thickness, peaking at 8 nm, which suggests enhanced magneto-optical response due to greater light absorption and interaction with the magnetic film.

The observed decrease in $H_c$ for the 10 nm sample may result from strain relaxation[67], changes in domain structures[68, 69], or a transition from interface-dominated behavior to bulk-like properties. In thinner films, interfacial effects and substrate-induced strain can enhance magnetic anisotropy, increasing $H_c$. However, as thickness increases, strain may partially relax, reducing magnetic anisotropy and leading



doi:10.6342/NTU202501047

to a lower coercivity. Additionally, thinner samples often exhibit stronger domain pinning effects due to rougher interfaces, whereas thicker films can develop more continuous domain structures, facilitating easier magnetization reversal.

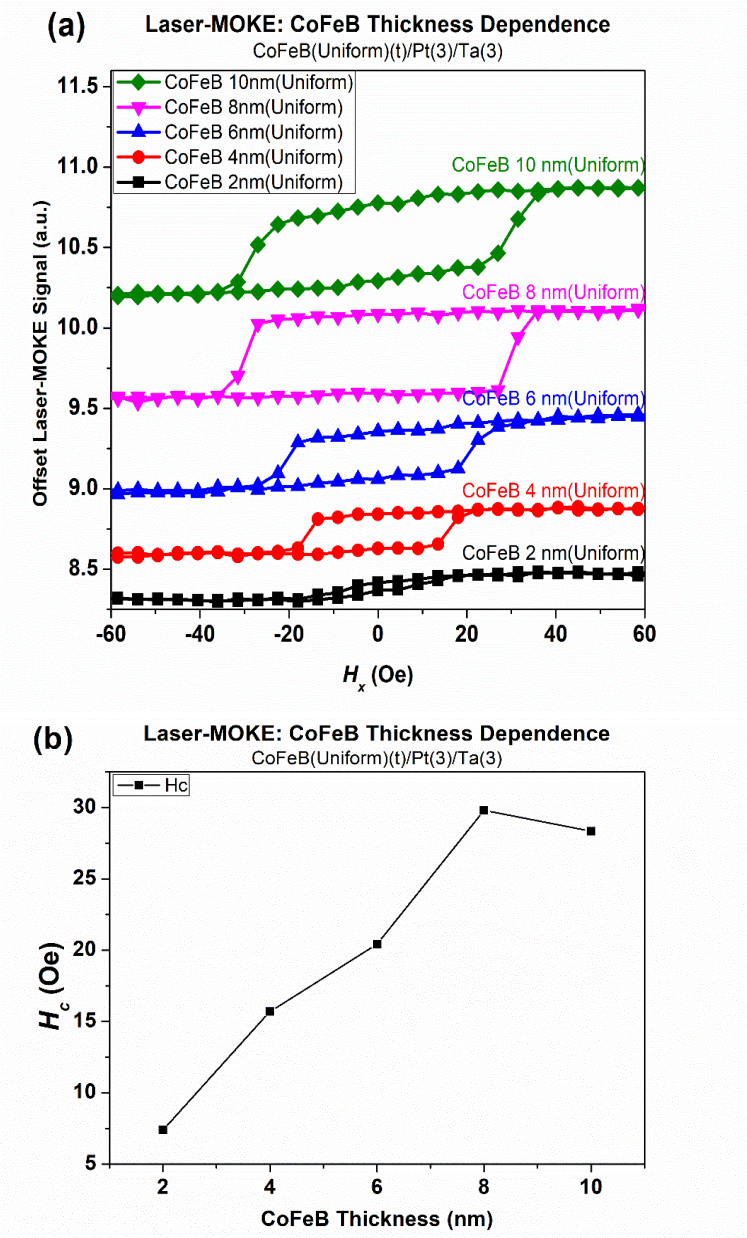


**Figure 3. 1** Laser-MOKE results of uniform CoFeB samples: (a) hysteresis loops and (b) coercivity ($H_c$) as a function of CoFeB thickness.



doi:10.6342/NTU202501047

This thickness-dependent study serves as a control experiment to establish reference samples for further investigations. Based on these results, the 6 nm and 8 nm samples were selected for subsequent experiments, as they exhibit well-defined magnetic properties suitable for further characterization.

## 3-1.2 Uniform Samples Angle Dependence

To further investigate the magnetic behavior of uniform samples, we performed angle-dependent MOKE measurements on CoFeB 6 nm (Uniform) and CoFeB 8 nm (Uniform) samples. The extracted coercivity ($H_c$) and remanent magnetization ratio ($M_r/M_s$) were plotted as polar diagrams (**Figure 3. 2**). Ideally, for a completely uniform thin film, both $H_c$ and $M_r/M_s$ should exhibit isotropic behavior, forming perfect circles in the polar plots. However, our results show a weak uniaxial anisotropy, where the $H_c$ variation follows an elliptical shape, while $M_r/M_s$ exhibits a butterfly-like or dumbbell-shaped distribution.



doi:10.6342/NTU202501047

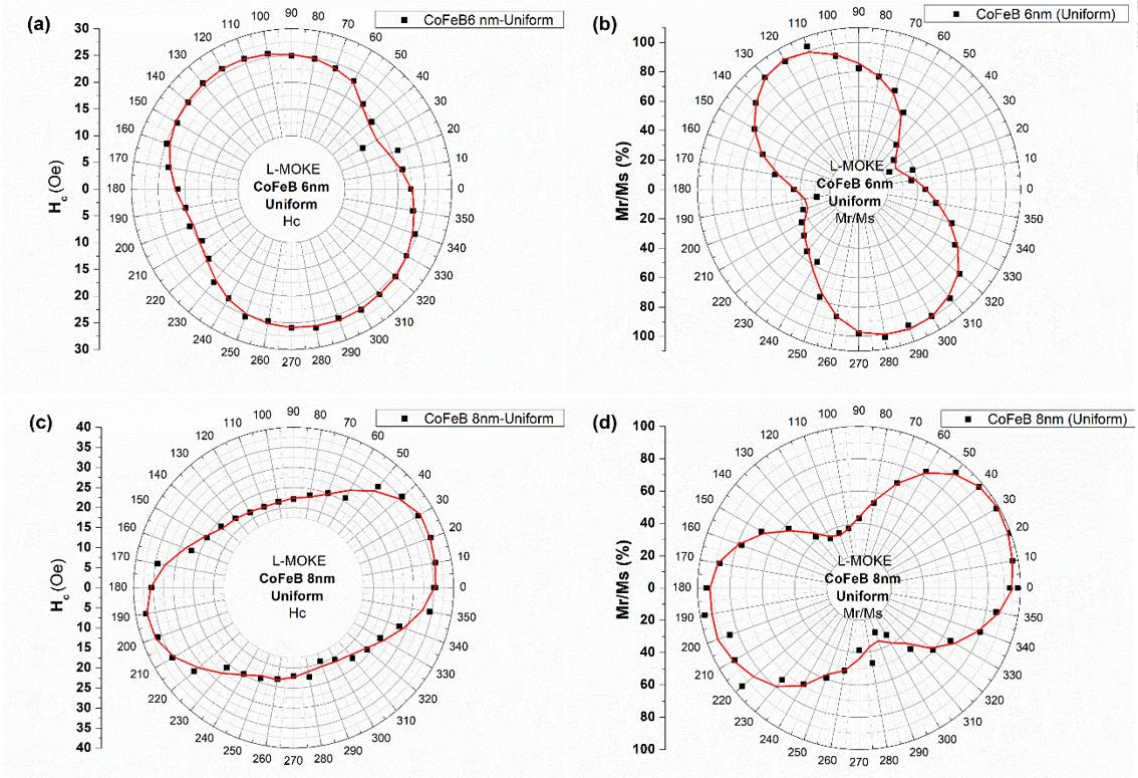


**Figure 3. 2** Polar diagrams of coercivity ($H_c$) and squareness ratio ($M_r/M_s$) for (a)(b) CoFeB 6nm (uniform) and (c)(d) CoFeB 8nm (uniform) samples.

This unexpected uniaxial anisotropy is likely due to residual stress introduced during the sputtering process[70-72]. Even though rotary motion was enabled during deposition to enhance uniformity, slight non-uniformities could still result in directional strain, influencing the magnetic anisotropy[73, 74]. Another possible origin is the substrate effect—since no seed layer was used, the film grew directly on the substrate, making it more susceptible to surface-induced strain[75, 76] or texture effects[77]. The sample shape might also contribute, as elongated or asymmetrical shapes can introduce form-induced anisotropy. However, this anisotropy does not exhibit a consistent preferred



doi:10.6342/NTU202501047

direction across different samples, suggesting that the effect is subtle and not driven by an external alignment field.

It is important to note that the purpose of this experiment was not to study the intrinsic anisotropy of uniform CoFeB films but rather to establish these samples as control references for later comparisons. The presence of weak anisotropy in the uniform samples serves as a baseline, allowing us to more clearly assess the enhanced anisotropy observed in the wedge samples, which will be discussed in the following sections.

## 3-1.3 Wedged-Shape Samples Angle Dependence

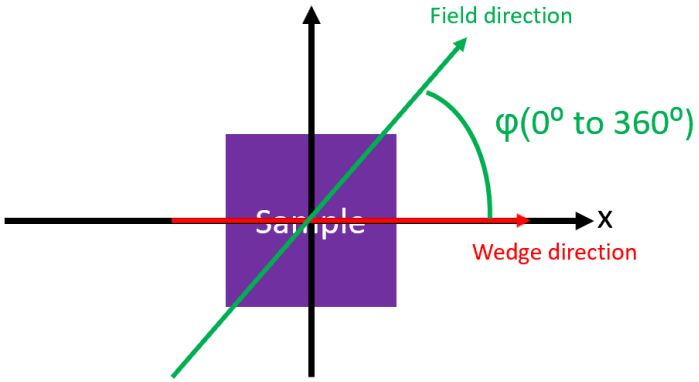


**Figure 3. 3** Measurement geometry of MOKE angle scan

In the Laser-MOKE angle-dependent measurements of CoFeB 6nm(Wedge) and CoFeB 8nm(Wedge) samples, a strong uniaxial anisotropy was observed, with the easy axis aligning with the deposition direction, confirming that Wedge Deposition induces significant anisotropy[28, 29]. Compared to uniform samples, the $H_c$ and $M_r/M_s$



doi:10.6342/NTU202501047

variations were much more pronounced, with $H_c$ changes exceeding 100 Oe. Furthermore, $H_c$ was consistently higher in the CoFeB 8nm(Wedge sample) than in the 6 nm one, following the same trend observed in the thickness dependence study. Additionally, $H_c$ increased as the field angle approached the hard axis (perpendicular to the wedge direction). Interestingly, the measured coercivity shows a clear angular dependence following an $H_c \propto \sec(\varphi)$ behavior, where $\varphi$ is the angle between the applied field and the easy axis. This trend deviates from the typical prediction of the coherent rotation model[78, 79], which expects the lowest $H_c$ near the hard axis. A possible explanation is that, under our measurement conditions, magnetization reversal is constrained along the easy axis[80, 81]. Since the Laser-MOKE setup operates at relatively low field strengths—and the observed $H_c$ is much smaller than the anisotropy field (as later confirmed by ST-FMR and FMR results)—the applied field is insufficient to significantly tilt the magnetization away from its preferred axis. As a result, reversal likely occurs when the projection of the external field onto the easy axis reaches a critical value. However, due to the limited field strength of the MOKE system, the component of the applied field along the easy axis becomes insufficient near the hard axis, preventing full magnetization reversal at these angles. This explains the absence of switching at 90°



doi:10.6342/NTU202501047

and 270° for the CoFeB 6nm(Wedge) sample, and the broader angular ranges (60–120° and 250–290°) for the CoFeB 8nm(Wedge) sample.

Consequently, the $M_r/M_s$ values approach zero at these angles, resulting in a more pronounced "butterfly" shape in the $M_r/M_s$ polar plot and a sharper angular variation in $H_c$ compared to the uniform samples.

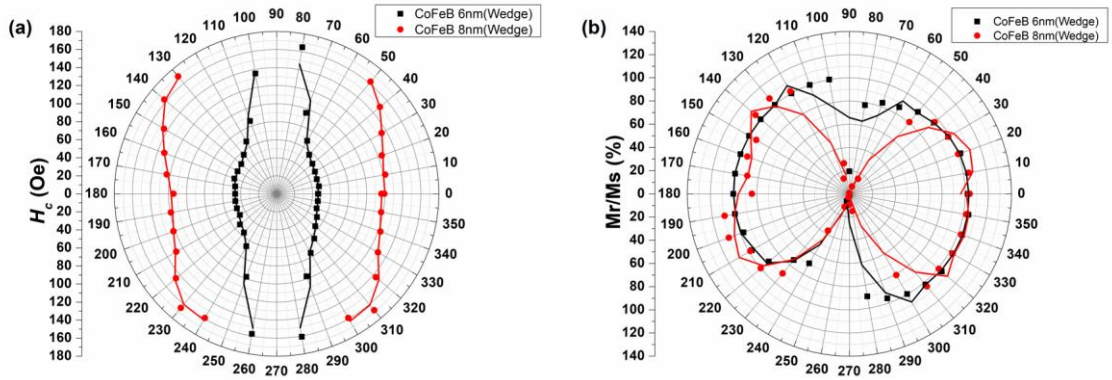


**Figure 3. 4** Polar diagrams of coercivity ($H_c$) and squareness ratio ($M_r/M_s$) for (a) CoFeB 6nm (Wedged) and (b) CoFeB 8nm (Wedged).



doi:10.6342/NTU202501047

# 3-2 VSM

For the Uniform samples, the VSM results were consistent with MOKE, with weak magnetic anisotropy, as shown in **Figure 3. 5**. The VSM measurements of CoFeB 6nm and 8nm Wedge samples (Wedge deposition angle = 0°) confirmed that the easy-axis hysteresis loop appears at 0°, while the hard-axis behavior is observed at 90° (**Figure 3. 5**). Further angular-dependent measurements of $M_r/M_s$ at 30° intervals (**Figure 3. 5**) revealed a trend consistent with the MOKE results. However, unlike in MOKE, the coercivity ($H_c$) did not exhibit significant angular dependence in VSM measurements.

This difference likely originates from the higher magnetic field range used in VSM (±8000 Oe), which exceeds the anisotropy field of the samples (as will be shown in the FMR and ST-FMR results). Under such strong fields, magnetization reversal is no longer restricted to occur along the easy axis, and the switching mechanism may transition to domain wall motion[82]. This could effectively mask the angular dependence of $H_c$.

Nevertheless, both the $M_r/M_s$ trend and the hysteresis loop shapes confirm that the easy axis aligns with the wedge deposition direction—consistent with MOKE results. This confirms that wedge deposition induces a well-defined uniaxial anisotropy in the films.



doi:10.6342/NTU202501047

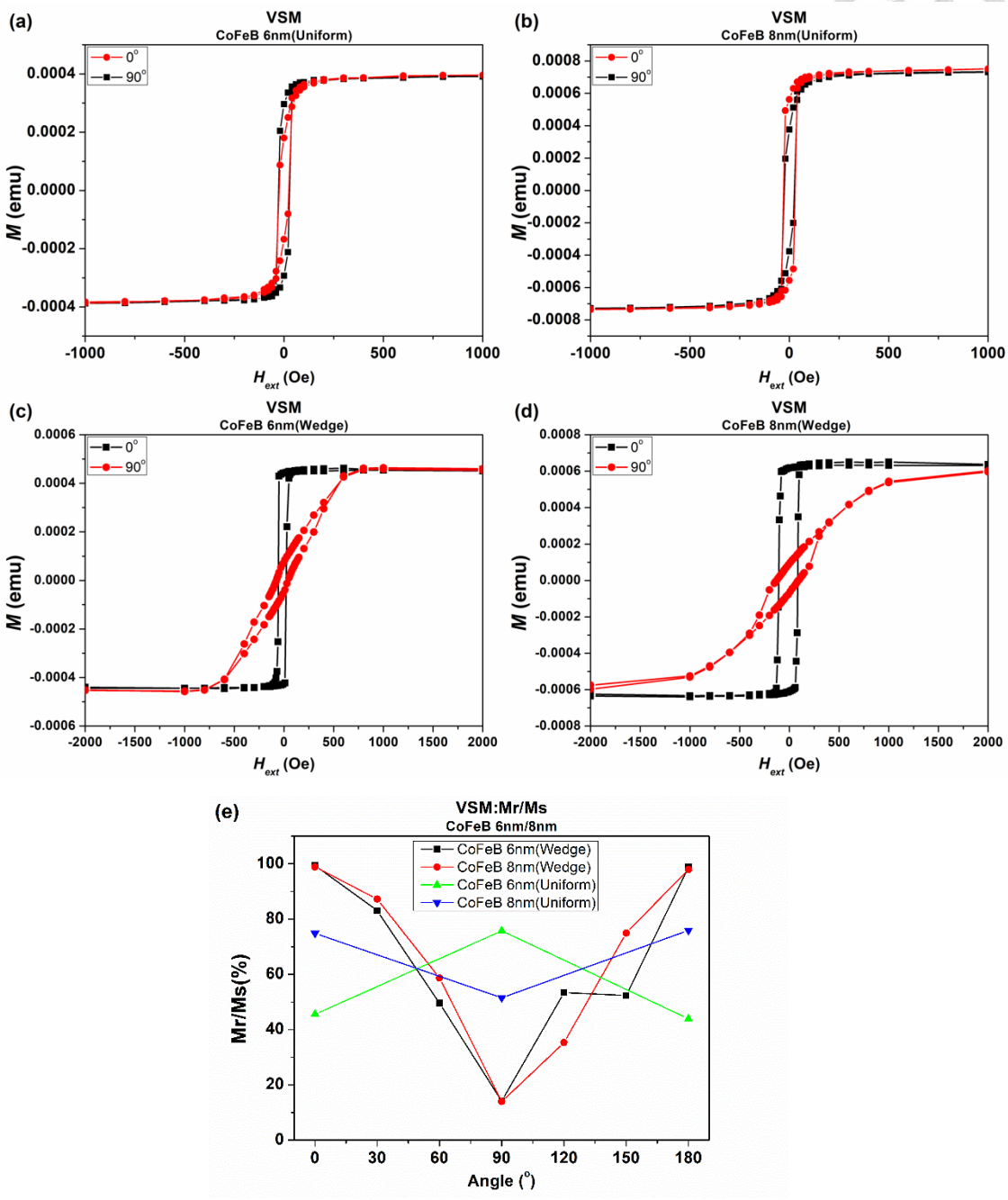


**Figure 3. 5** VSM results of (a) CoFeB 6nm(Uniform), (b) CoFeB 8nm(Unifrom), (c) CoFeB 6nm (Wedge) and (d) CoFeB 8nm (Wedge) measured along the easy and hard axes, and (e) angular dependence of the squareness ratio ($M_r/M_s$).



doi:10.6342/NTU202501047

# 3-3 ST-FMR: Frequency Dependence

ST-FMR measurements were performed to extract the effective demagnetization field ($4\pi M_{\text{eff}}$) and damping constant ($\alpha$). The results are analyzed separately for Uniform and Wedged samples to examine the impact of Wedge deposition on these magnetic properties.

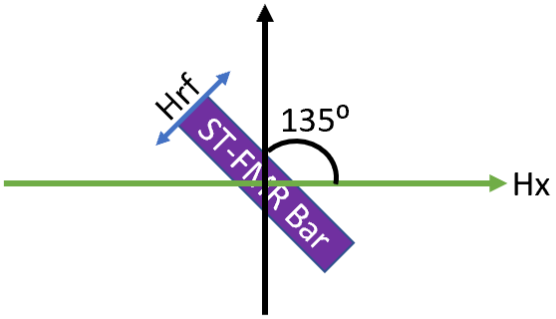


**Figure 3. 6** Measurement configuration of ST-FMR frequency dependence.



doi:10.6342/NTU202501047

## 3-3.1 Uniform Samples

ST-FMR measurements were conducted on uniform CoFeB samples with different thicknesses, and the results were analyzed using Kittel formula fitting (**Figure 3. 7**) and damping constant fitting (**Figure 3. 7**). The extracted demagnetization field ($4\pi M_{eff}$) and damping constant ($\alpha$) are further plotted as a function of CoFeB thickness in **Figure 3. 7**.

The results show that the demagnetization field increases with CoFeB thickness, but the rate of increase slows as the thickness grows, which is consistent with previous studies[83, 84]. This trend is consistent with the behavior observed in MOKE hysteresis loops, where thicker CoFeB samples exhibited higher coercivity ($H_c$). The increase in $4\pi M_{eff}$ can be attributed to the larger magnetization volume, while the diminishing rate of change suggests an increasing influence of internal demagnetization effects.



doi:10.6342/NTU202501047

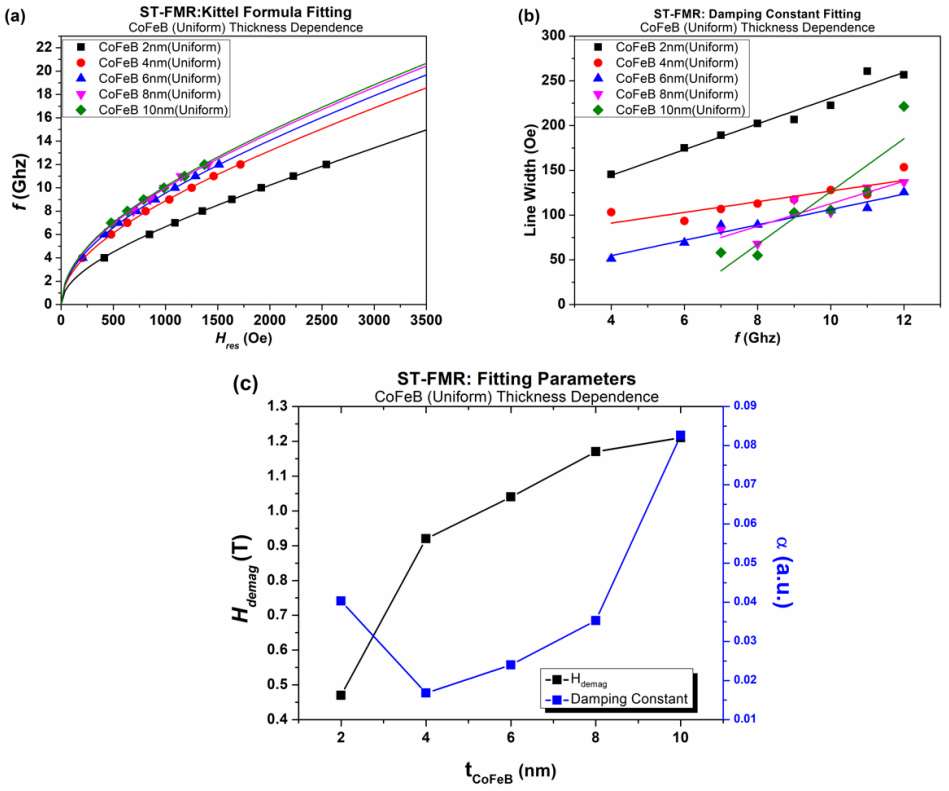


**Figure 3. 7** ST-FMR analysis of Uniform CoFeB samples, including (a) Kittel formula fitting, (b) damping constant fitting, and (c) extracted demagnetization field and damping constant.

For the damping constant, we observe a non-monotonic trend: α first decreases with increasing thickness, reaching a minimum at 4 nm, and then increases as the film becomes thicker. The initial decrease can be attributed to strong interface-related effects, such as spin-pumping[85, 86] and scattering at rough interfaces[87], which contribute more significantly to damping in thinner films due to their larger surface-to-volume ratio. As the film thickness increases, these interface effects diminish, while bulk-related mechanisms, including eddy-current losses[88] and two-magnon scattering[89, 90] from volume defects, become more prominent. The eddy-current contribution, which scales



doi:10.6342/NTU202501047

approximately with the square of the film thickness, and the enhanced magnon scattering within the film volume collectively leading to an increase in α at larger thicknesses. This thickness-dependent damping behavior has also been reported in other metallic ferromagnetic thin film systems[88].

## 3-3.2 Wedge-shaped Samples

ST-FMR measurements were performed on wedged CoFeB samples with different deposition angles to investigate the effects of wedge-induced anisotropy on the resonance behavior. The results are shown in **Figure 3. 9**, where Kittel formula fitting is presented in **Figure 3. 9**, and damping constant fitting is shown in **Figure 3. 9**.

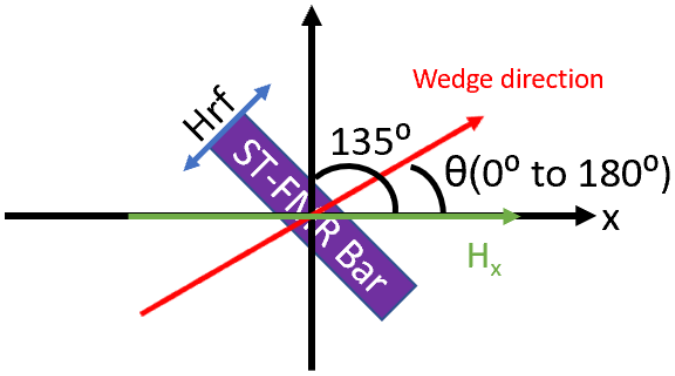


**Figure 3. 8** Measurement configuration of ST-FMR frequency dependence for wedge samples.



doi:10.6342/NTU202501047

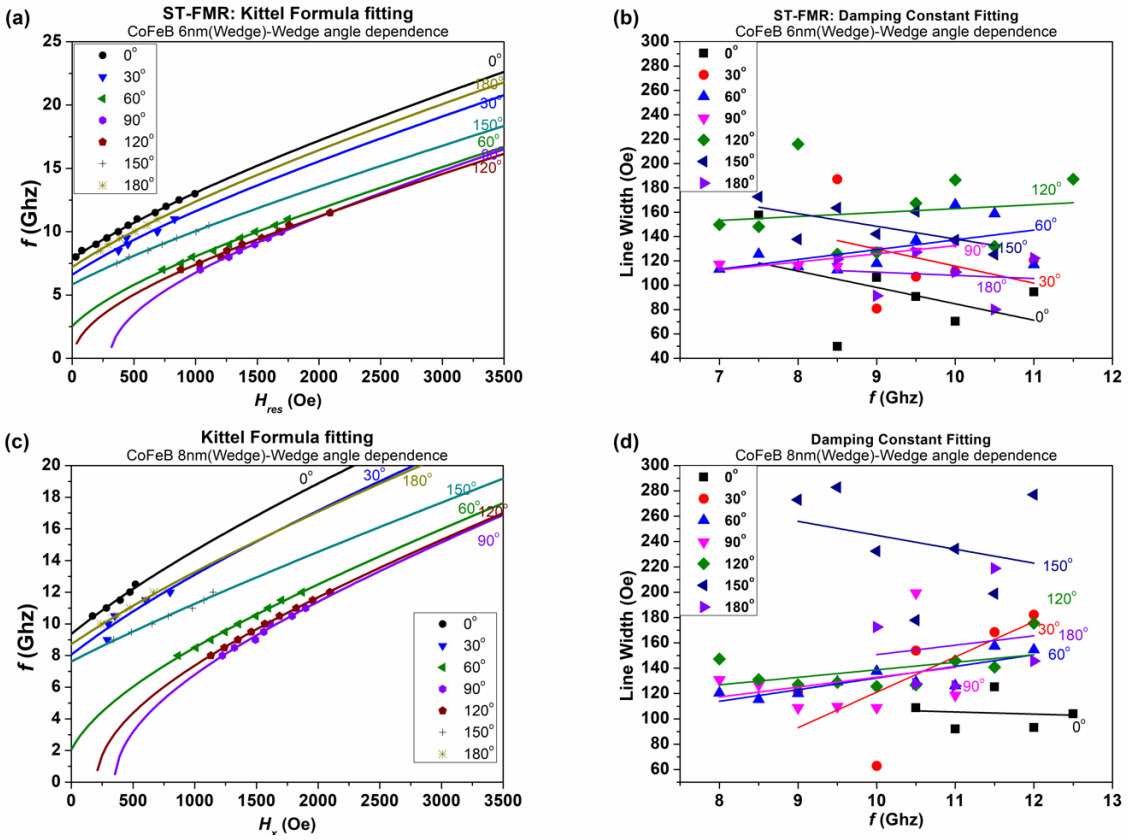


**Figure 3. 9** Kittel formula and damping constant fitting for (a)(b) CoFeB 6nm(Wedge) and (c)(d)CoFeB 8nm(Wedge).

Compared to uniform samples, fitting the experimental data using Kittel formula(**(1. 2)**) requires the inclusion of an anisotropy field term ($H_k$) to accurately describe the resonance condition. This indicates that wedge deposition significantly enhances uniaxial anisotropy, making $H_k$ much larger than that of uniform samples. This result is consistent with the MOKE and VSM findings, which also revealed strong anisotropic behavior in wedged samples. The increased anisotropy once again originates from the



doi:10.6342/NTU202501047

wedge deposition process, which induces a preferential in-plane anisotropy aligned with the wedge direction.

For the linewidth fitting, the frequency dependence in wedged samples deviates from the linear behavior typically expected from Gilbert damping. This irregular trend may result from multiple overlapping factors, including the strong uniaxial anisotropy induced by wedge deposition, the presence of a thickness gradient, and the shape anisotropy introduced during device patterning. These factors collectively complicate the magnetization dynamics and hinder the accurate extraction of intrinsic damping. Given the current experimental design, a precise analysis of the linewidth behavior remains challenging. Further investigation, such as angle-resolved FMR or micromagnetic simulations, would be required to disentangle these effects and clarify the underlying mechanisms.

To further examine the influence of wedge deposition on magnetic properties, the effective demagnetization field ($4\pi M_{eff}$) extracted from Kittel formula fitting was plotted against wedge angle. As shown in **Figure 3. 10**, the values of $4\pi M_{eff}$ remain relatively constant across different wedge angles and are comparable to those of uniform samples. In both the CoFeB 6nm(Wedge) and CoFeB 8nm(Wedge) series, the 8 nm samples exhibit slightly higher $4\pi M_{eff}$, consistent with the thickness-dependent trend



doi:10.6342/NTU202501047

observed in **Figure 3. 7**. This suggests that the wedge geometry primarily affects the in-plane anisotropy, while the demagnetization field remains largely unaffected.

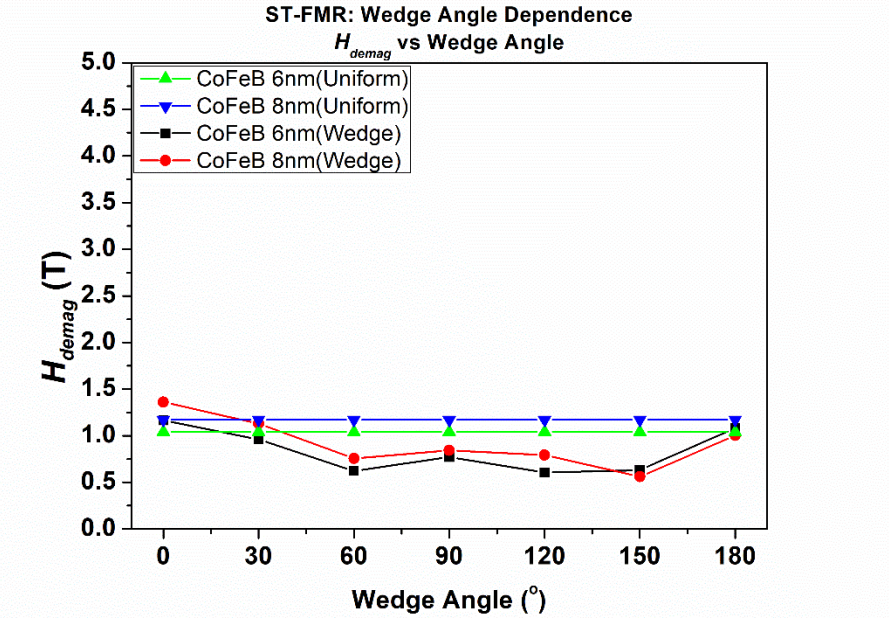


**Figure 3. 10** Demagnetization field for different wedge angles and uniform samples.

To further analyze the in-plane anisotropy induced by wedge deposition, the anisotropy field $H_k$ extracted from Kittel formula fitting was plotted as a function of wedge angle. The data were fitted using the empirical expression:

$$H_k = H_{k0} + H_u \cos 2(\theta - \varphi_{EA}) \quad \textbf{(3. 1)}$$

where $H_{k0}$ is the represents the baseline anisotropy field, $H_u$ is the magnitude of uniaxial anisotropy, and $\varphi_{EA}$ corresponds to the easy-axis direction. As shown in **Figure 3. 11**



doi:10.6342/NTU202501047

, the fitting results reveal a clear uniaxial anisotropy, with $H_u$ larger in the CoFeB 8nm(Wedge) sample compared to the 6 nm sample—consistent with the MOKE measurements. A summary of the fitting parameters is provided in **Table 3. 1**.

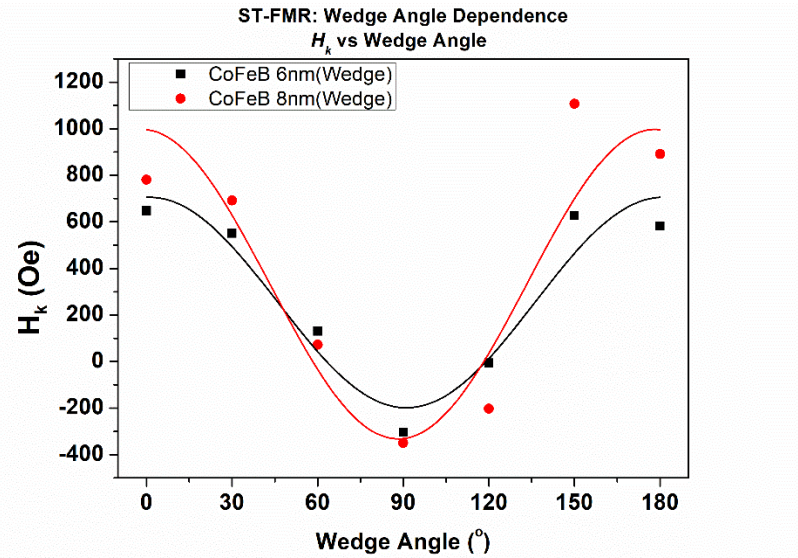


**Figure 3. 11** $H_k$ fitting based on Kittel formula for different wedge angles, with fitting using the expression $H_k = H_{k0} + H_u \cos 2(\theta - \varphi_{EA})$

| Sample | $H_{k0}$ (Oe) | $H_u$ (Oe) | $\varphi_{EA}$(°) |
|---|---|---|---|
| CoFeB 6nm(Wedge) | 253.46761 | 452.26635 | 1.08033 |
| CoFeB 8nm(Wedge) | 332.43126 | 664.9812 | -1.74553 |

**Table 3. 1** Fitting Parameters for Different Wedge Angles Based on Eq.3.1.

Interestingly, the fitted values of $H_{k0}$ show a non-zero offset: 253.5 Oe for CoFeB 6 nm and 332.4 Oe for CoFeB 8 nm. Since the angle-dependent ST-FMR measurements are performed on samples with fixed thickness, this shift in $H_k$'s baseline is unlikely to be caused by wedge-induced anisotropy alone. A more plausible explanation is the presence of shape anisotropy introduced during device fabrication. Specifically, the



doi:10.6342/NTU202501047

lithographically defined device geometry may introduce an additional directional anisotropy or cause a misalignment between the device axis and the actual wedge direction, leading to a systematic offset in $H_k$.

# 3-4 ST-FMR: Angle Scan

To further investigate the angular dependence of resonance behavior, we performed ST-FMR angle scans on both uniform and wedged series samples. For the uniform samples (only 6 nm and 8 nm), the external magnetic field was rotated in 30° steps over a full 360° range. In contrast, for the wedged samples (with a wedge angle of 0°), the field was scanned in finer 10° steps to capture detailed angular variations.

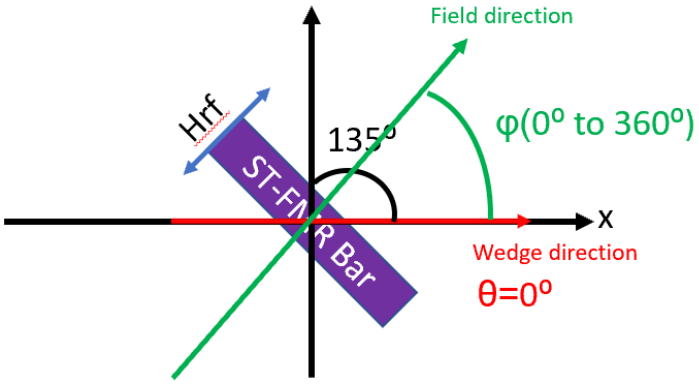


**Figure 3. 12** Measurement configuration of ST-FMR Angle Scan.

The extracted resonance fields ($H_{res}$) are shown in **Figure 3. 13** for the uniform samples and **Figure 3. 14** for the CoFeB 6nm(Wedge) and CoFeB 8nm(Wedge) sample, respectively.



doi:10.6342/NTU202501047

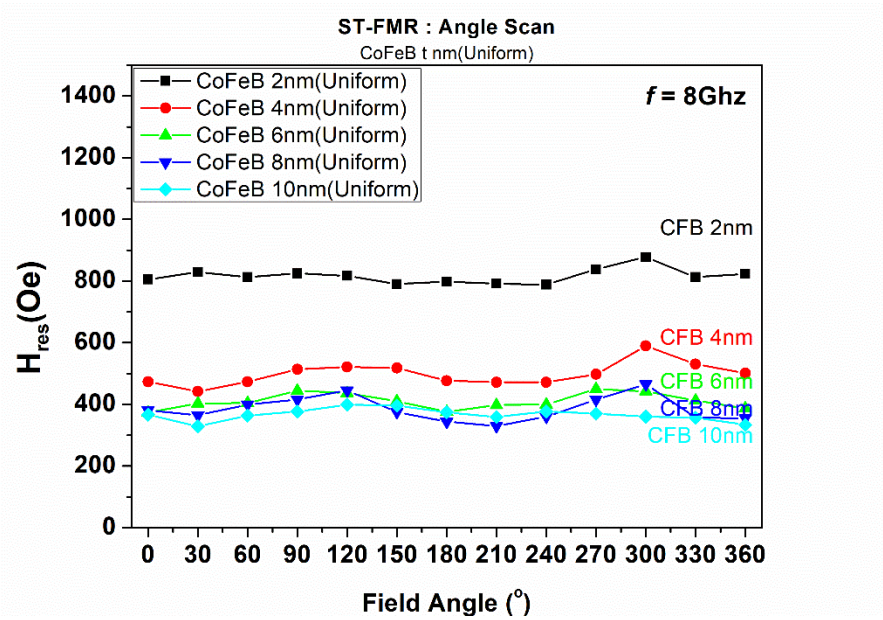


**Figure 3. 13** Resonant Field vs. Field Angle for Uniform Series Samples at 8 GHz.

As shown in **Figure 3. 13**, the resonance fields of the uniform samples remain nearly constant with respect to field angle, consistent with the weak or negligible anisotropy observed earlier. In contrast, the wedged samples exhibit a clear angular dependence that follows a $\cos 2(\theta - \varphi_{EA})$ trend, consistent with a strong uniaxial anisotropy. This behavior is well described by the fitting function[28, 83]:

$$H_{res}(\theta) = H_0 - H_u \cos 2(\theta - \varphi_{EA}) \quad \textbf{(3. 2)}$$

Here, $H_{res}$ is the measured resonance field, $H_0$ represents the baseline resonance field due to the film's intrinsic properties, $H_u$. is the contribution from the uniaxial anisotropy field, and $\varphi_{EA}$ denotes the angle of the easy axis. It is important to note the difference in the physical context between the Kittel formula fitting (**(3. 1)**) and the angular scan fitting. In **(3. 1)**, the extracted anisotropy field $H_k$ represents the component of the anisotropy



doi:10.6342/NTU202501047

field along the direction of the applied field (x-axis). As a result, $H_k$ reaches its maximum when the wedge direction (i.e., the easy axis) is aligned with the external field direction, justifying the use of a positive sign in **(3. 1)**. In contrast, the angular scan measures how the resonance field varies with the angle of the applied field. This variation arises from the interplay between the applied field and the anisotropy field. When the field is aligned with the easy axis, the resonance condition is satisfied with a smaller external field due to the alignment of the magnetization and anisotropy field. Near the hard axis, a stronger external field is required to overcome the anisotropy and rotate the magnetization away from the easy axis, resulting in a higher resonance field. To reflect this behavior, the fitting formula adopts a negative sign in **(3. 2)** This convention ensures that the extracted $H_u$ remains positive and physically meaningful.

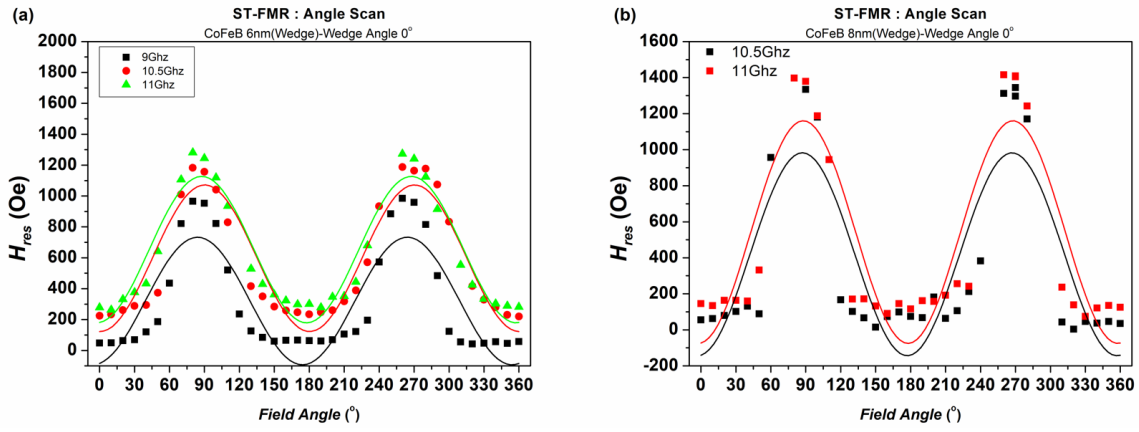


**Figure 3. 14** Resonant Field vs. Angle for wedge series samples measured by ST-FMR Angle Scan, with fitting using Eq3.2



doi:10.6342/NTU202501047

The fitting parameters are summarized in **Table 3. 2** The extracted $H_u$ values are consistent with earlier results, again confirming that CoFeB 8 nm exhibits a stronger anisotropy than 6 nm. Moreover, the fitted easy axis directions align well with the deposition direction, further supporting that the anisotropy originates from the wedge deposition process.

| Sample | frequency | $H_0$(Oe) | $H_u$(Oe) | $\varphi_{EA}$(°) |
|---|---|---|---|---|
| CoFeB 6nm(Wedge) | 9Ghz | 320.07731 | 412.86241 | -5.81196 |
| | 10.5Ghz | 597.23041 | 474.8802 | 0.26702 |
| | 11Ghz | 653.20343 | 474.04091 | -2.42019 |
| CoFeB 8nm(Wedge) | 10.5Ghz | 419.69371 | 563.33438 | -2.88534 |
| | 11Ghz | 542.78332 | 618.0541 | -2.18566 |

**Table 3. 2** Fitting Parameters from Resonant Field vs. Angle Data

The ST-FMR angle scan measurements primarily serve to quantify the magnitude of the wedge-induced anisotropy. The observed directional variation in $H_{res}$, well described by a $\cos2(\theta - \varphi_{EA})$ dependence, enables the extraction of the uniaxial anisotropy field $H_u$. The increasing $H_u$ values with CoFeB thickness are consistent with trends observed in earlier MOKE and ST-FMR wedge angle dependence results, providing complementary quantitative insight into the anisotropy strength.



doi:10.6342/NTU202501047

# 3-5 FMR: Frequency Dependence

To further verify the consistency of our observations, we performed frequency-dependent ferromagnetic resonance (FMR) measurements on unpatterned CoFeB samples (6 nm and 8 nm, both uniform and wedged). The magnetic field was applied at various in-plane angles from 0° to 180° in 30° steps to examine whether the frequency response varies with field orientation. From these measurements, the effective demagnetization field ($4\pi M_{eff}$), damping constant (α), and anisotropy field ($H_k$) were extracted and analyzed, serving as a complementary validation to the previous ST-FMR results.

**Figure 3. 15** shows the Kittel formula fitting results. Similar to the ST-FMR results, the uniform samples exhibit negligible angular dependence of the fitted parameters. In contrast, the wedged samples show significant angle-dependent behavior, indicating the presence of strong uniaxial anisotropy.



doi:10.6342/NTU202501047

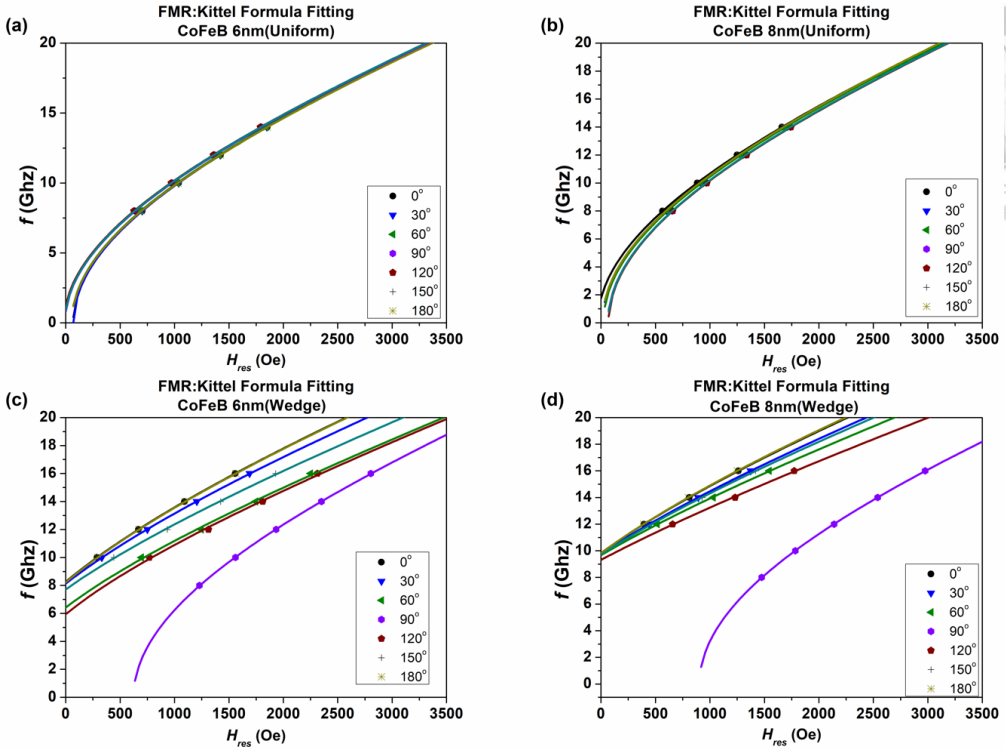


**Figure 3. 15** Kittel Formula Fitting for (a)(b) Uniform Samples and (c)(d) Wedge-Shape Samples.

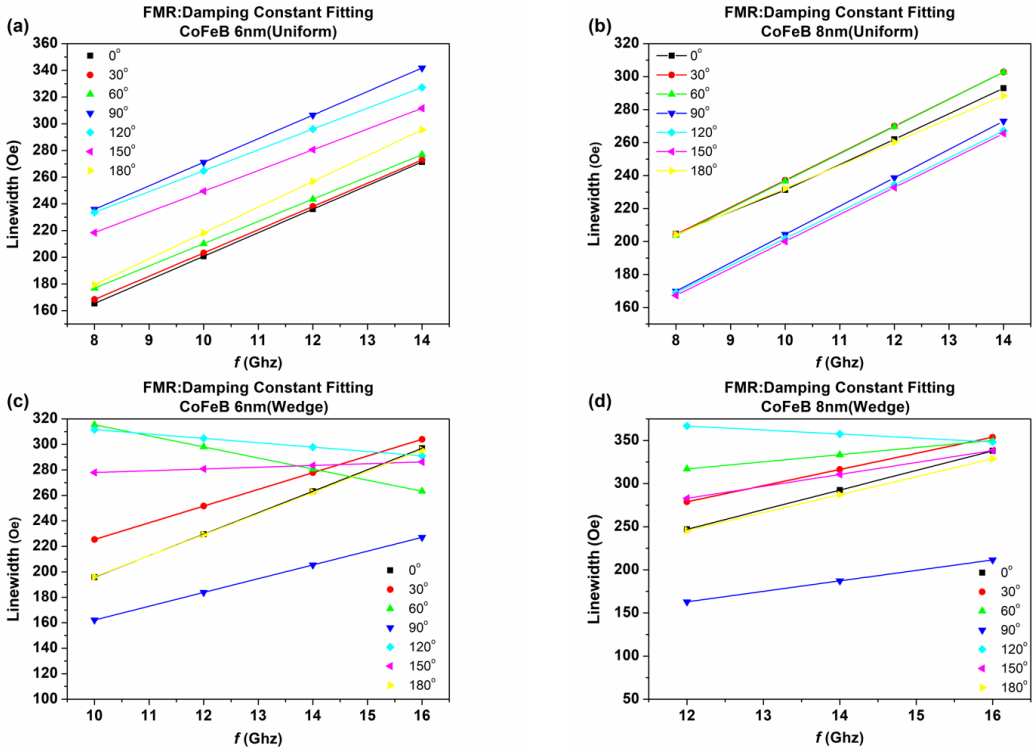


**Figure 3. 16** Damping constant fitting for (a)(b) uniform samples and (c)(d) wedge-shape samples.



doi:10.6342/NTU202501047

The linewidth vs. frequency fitting results are presented in **Figure 3. 16**. For the uniform samples, the linewidths remain linearly dependent on frequency across all angles, with little variation in the extracted damping constants. In contrast, the wedged samples show more pronounced angular dependence. This angular dependence of linewidth is likely related to the strong uniaxial anisotropy introduced by wedge deposition, which affects precession dynamics and complicates the linewidth behavior.

A more detailed comparison of the angular dependence is summarized below.

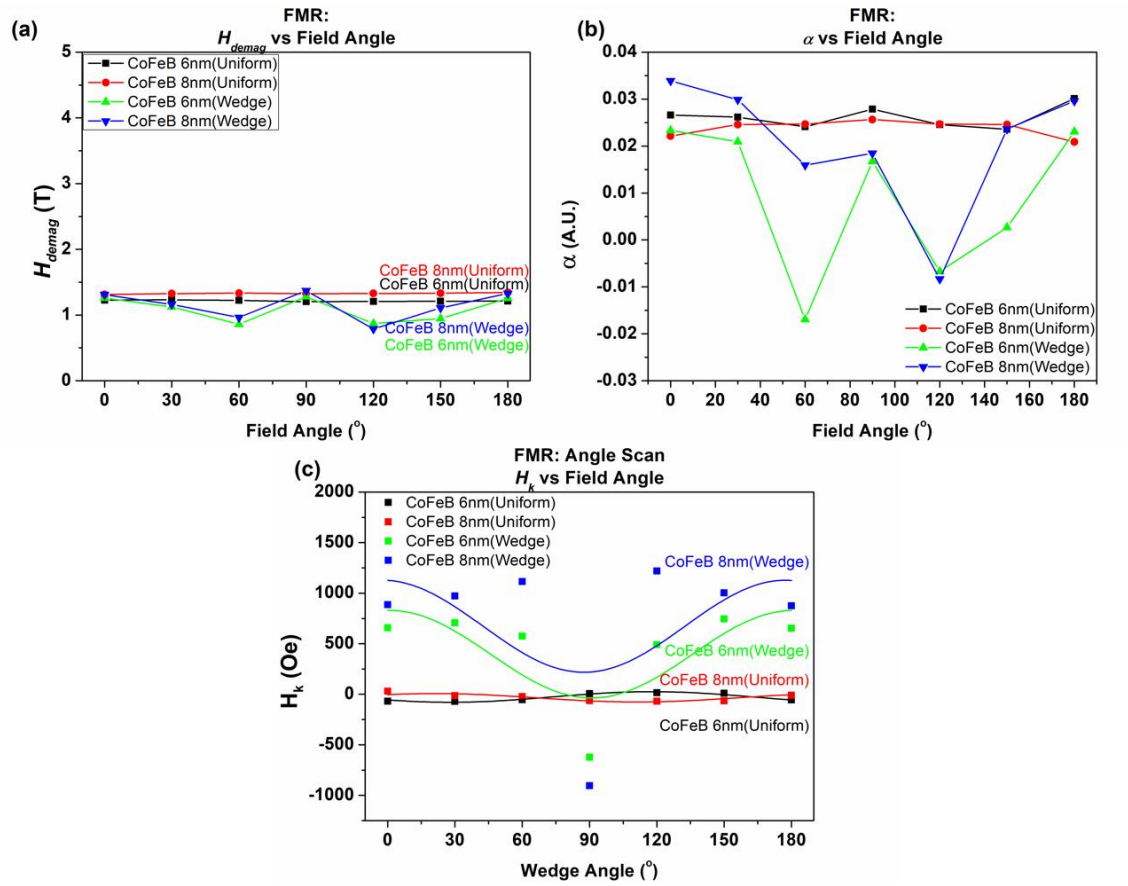


**Figure 3. 17** Fitting parameters of FMR: (a) Demagnetization Field,(b) Damping Constant,(c)$H_k$



doi:10.6342/NTU202501047

**Figure 3. 17** summarizes the extracted fitting parameters. In panel (a), the demagnetization fields are plotted, showing consistent trends with the ST-FMR results. The CoFeB 8 nm samples consistently exhibit slightly larger $4\pi M_{eff}$ values than CoFeB 6nm samples. Furthermore, the wedge samples exhibit only slight angular variation, and the values remain close to 1 T, suggesting minimal influence from the wedge on the demagnetization field. Panel (b) shows the damping constants in different field angle. The uniform samples again display stable values across angles, while the wedge samples show more fluctuation. Notably, damping values near the easy (0°, 180°) and hard (90°) axes tend to be more stable and closer to those of uniform films, while values at intermediate angles can deviate significantly—consistent with the drag effect [91-93], where strong uniaxial anisotropy causes the precession dynamics to become more complex specifically when the applied field is not aligned with the anisotropy axes. In these off-axis conditions, the resonance linewidth often exhibits a nonlinear dependence on frequency, leading to unreliable damping extraction from linear fits. Therefore, only the damping values measured along the easy and hard axes are considered reliable and physically meaningful. Finally, panel (c) presents the fitted $H_k$ values. As with the ST-FMR analysis, the uniform samples yield $H_k$ values centered around zero with negligible angular dependence. In the wedged samples, $H_k$ varies with angle,



doi:10.6342/NTU202501047

though unlike the ST-FMR results, the angular dependence does not closely follow a clear cos(2θ) trend. This discrepancy may be due to the lack of lithographic patterning in the FMR samples, meaning that their overall magnetic anisotropy is still influenced by the macroscopic sample shape. Nonetheless, by comparing the range (maximum–minimum) of $H_k$, we still observe that the 8 nm samples consistently show stronger anisotropy than the 6 nm samples.

Moreover, in contrast to the ST-FMR data, the FMR results do not show any offset in the angular dependence of $H_k$ —the variation is symmetric about 0°. This supports the hypothesis that the offset observed in ST-FMR (i.e., non-zero $H_{k0}$) originates from additional anisotropy induced by device patterning, such as shape anisotropy introduced during microfabrication.



doi:10.6342/NTU202501047

# 3-6 FMR: Angle Dependence

In this section, we analyze the angular dependence of the resonance field ($H_{res}$) for both Uniform and Wedge samples, with the measurement configuration shown in **Figure 3. 18**.

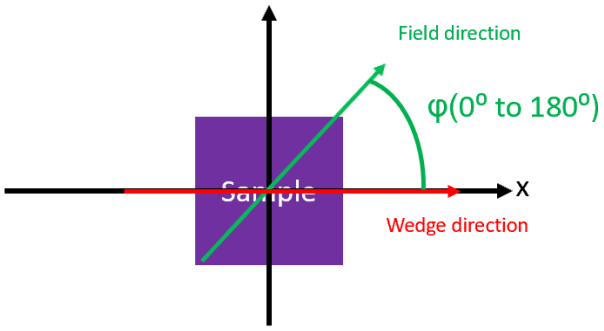


**Figure 3. 18** Measurement configuration of FMR angle dependence.

The Uniform samples were measured at four different frequencies (8, 10, 12, and 14 GHz), with the results presented in **Figure 3. 19**. The Wedge samples were measured at slightly higher frequencies: **Figure 3. 19** shows the data for the 6 nm sample (measured at 10, 12, 14, and 16 GHz), and **Figure 3. 19** presents the 8 nm sample (measured at 12, 14, and 16 GHz).



doi:10.6342/NTU202501047

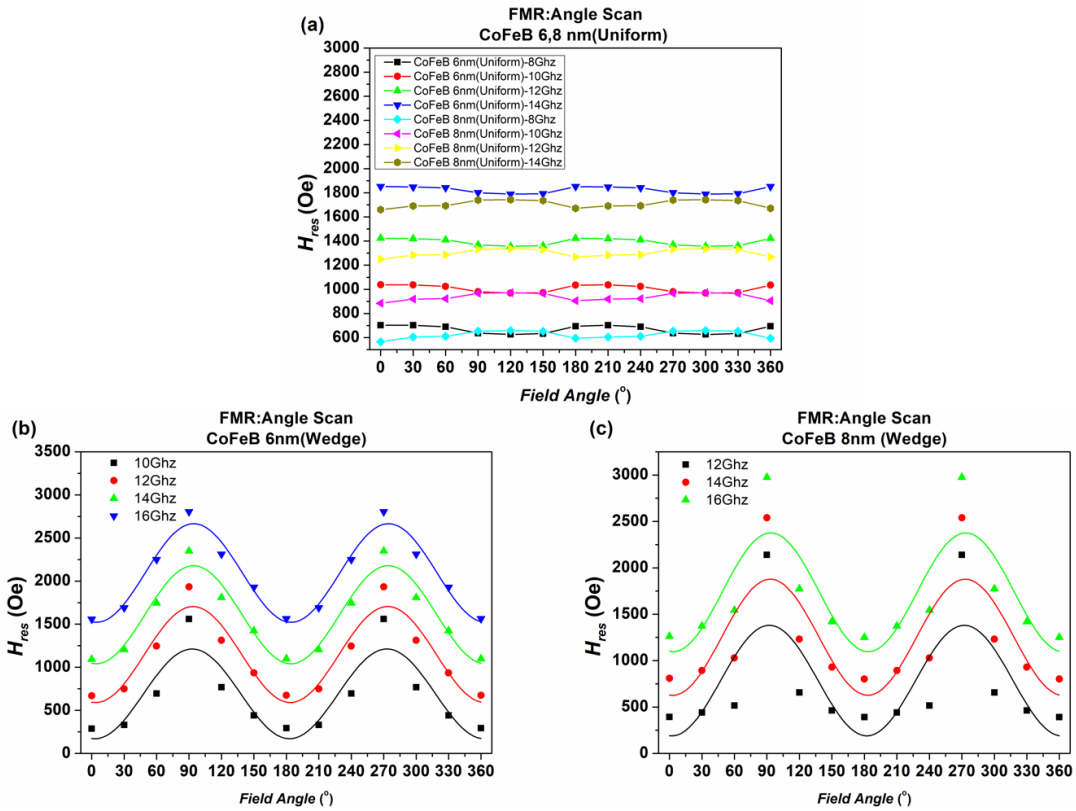


**Figure 3. 19** FMR Angle Scan Results: (a) Uniform Samples, (b) CoFeB 6nm (Wedge), (c) CoFeB 8nm (Wedge).

For all samples, the extracted resonance fields ($H_{res}$) were fitted using the same fitting model applied in the ST-FMR angle scan section(**(3. 2)**) The fitted values of $H_u{}'$ are summarized in **Table 3. 3**.

| Sample | frequency | $H_0$(Oe) | $H_u$(Oe) | $\varphi_{EA}$(°) |
|---|---|---|---|---|
| CoFeB 6nm(Wedge) | 10 Ghz | 691.44609 | 520.84612 | 2.90971 |
| | 12 Ghz | 1147.98093 | 557.77712 | 3.70627 |
| | 14 Ghz | 1609.59946 | 570.01394 | 4.15125 |
| | 16 Ghz | 2094.17303 | 572.28378 | 4.39563 |
| CoFeB 8nm(Wedge) | 12 Ghz | 785.2505 | 595.73711 | 2.2489 |
| | 14 Ghz | 1252.37122 | 626.07334 | 3.16222 |
| | 16 Ghz | 1736.05091 | 640.42956 | 3.57072 |

**Table 3. 3** Fitting Parameters from FMR Angle Scan



doi:10.6342/NTU202501047

For the uniform samples, the resonance field showed minimal angular dependence, consistent with the ST-FMR angle scan results. Consistent with earlier ST-FMR results, the wedge samples displayed clear angular dependence in the resonance field. The extracted $H_u$ values were higher in the 8 nm samples, indicating stronger anisotropy with increasing thickness.

The extracted $H_u$ values exhibited an increasing trend with frequency for both CoFeB 6 nm and 8 nm wedge samples, but this trend gradually saturated at higher frequencies. This apparent frequency dependence is primarily attributed to fitting sensitivity rather than a genuine change in anisotropy. At lower frequencies, the $H_{res}$ is closer in magnitude to the anisotropy field, which reduces the angular sensitivity of the resonance condition due to the nonlinear square-root dependence in the Kittel equation. As a result, angular modulation in $H_{res}$ becomes less pronounced, leading to increased uncertainty in the extraction of $H_u$. In contrast, at higher frequencies where $H_{res}$ is significantly larger than the anisotropy field, the angle-dependent variation of $H_{res}$ becomes more apparent, enabling more reliable fitting of $H_u$. These observations are consistent with ST-FMR results, reinforcing the understanding that $H_u$ itself remains frequency-independent.



doi:10.6342/NTU202501047

The fitted easy axis angles ($\varphi_{EA}$) for the Wedge samples were centered around 0°, consistent with the measurement geometry, as the samples were aligned such that the wedge direction lay along the 0° axis.

In summary, these observations confirm that the angular dependence of the resonance field reflects the influence of the wedge-induced anisotropy, with $H_u$ values following the expected trend of increasing with frequency and showing consistent behavior with both the angular and frequency-dependent measurements.



doi:10.6342/NTU202501047

# 3-7 Comparison between FMR and ST-FMR

One of the key differences between FMR and ST-FMR lies in the sample preparation process. ST-FMR requires patterning the films into well-defined devices (ST-FMR bars). While this approach helps reduce sample-to-sample variation and enhances signal quality, it also introduces additional shape anisotropy. This can lead to slight distortion in the extracted magnetic properties—for instance, the fitted $H_k$ values in ST-FMR often show a shift (offset), likely due to this added anisotropy from the patterned geometry.

In contrast, FMR measurements can be performed without any patterning. This offers several advantages: the fabrication process is simpler and more cost-effective, and since the sample remains unaltered during measurement, it can be reused for other experiments or fabrication steps. However, in this work, our FMR measurements were performed on unpatterned sample fragments without controlled shape. As a result, some degree of shape anisotropy was still observed during the measurement. This could be improved in the future by designing and fixing the sample geometry more carefully to minimize shape-induced effects and improve measurement accuracy.

Another notable point of comparison is the angular dependence measurement. In ST-FMR, the signal strength varies with the angle between the magnetic field and the ST-FMR bar due to the relative alignment between the RF current and the external field. This



doi:10.6342/NTU202501047

limits the range of measurable frequencies in angle-resolved measurements. On the other hand, in FMR measurements, the RF magnetic field—delivered through a waveguide—is always perpendicular to the external field. This ensures efficient excitation of the sample's magnetization at all field angles, allowing for more consistent signal quality and enabling angle-dependent measurements over a broader frequency range. As a result, more reliable extraction of the damping constant and resonance fields (via Kittel formula fitting) is possible in FMR.

It's worth noting that ST-FMR also provides access to spin-orbit torque (SOT) related properties, which is an important advantage. However, this lies outside the scope of the present study.

To better compare the results obtained from FMR and ST-FMR measurements, **Table 3. 4** summarizes the key extracted parameters—including the demagnetization field, damping constant, effective anisotropy field $H_k$, and uniaxial anisotropy field $H_u$—for each sample. This overview provides a direct comparison between the two methods in terms of both magnitude and angular trends. A more detailed discussion follows.

Despite these methodological differences, the results obtained from FMR and ST-FMR in this work are comparable. A summary table is provided to compare key



doi:10.6342/NTU202501047

parameters both methods. While some numerical discrepancies exist, the overall trends and characteristics are consistent. This consistency suggests that both techniques are valid and valuable for studying the magnetic properties of thin films.

| Parameter | Sample | ST-FMR | FMR |
|---|---|---|---|
| Demagnetization Field ($4\pi M_{eff}$)(T)(Average) | CoFeB 6nm(Uniform) | 1.04 | 1.2162 |
| | CoFeB 8nm(Unifom) | 1.17 | 1.3287 |
| | CoFeB 6nm(Wedge) | 0.833697 | 1.0842 |
| | CoFeB 8nm(Wedge) | 0.920671 | 1.1473 |
| $\triangle H_k$ (Oe) | CoFeB 6nm(Uniform) | -13.88885 | -52.19781 |
| | CoFeB 8nm(Unifom) | -15.95504 | 41.42652 |
| | CoFeB 6nm(Wedge) | 452.26635 | 433.15508 |
| | CoFeB 8nm(Wedge) | 664.9812 | 454.85772 |
| Fitted $H_u$ (Oe) | CoFeB 6nm(Uniform) | 31.85517 | -52.19781 |
| | CoFeB 8nm(Unifom) | 46.16665 | 41.42652 |
| | CoFeB 6nm(Wedge) | 453.9278 | 555.2302 |
| | CoFeB 8nm(Wedge) | 590.694 | 620.7467 |

**Table 3. 4** Comparison of Fitting Parameters from ST-FMR and FMR



doi:10.6342/NTU202501047

# IV. Conclusion

In this study, we systematically investigated the magnetic anisotropy behavior in CoFeB thin films with different thicknesses (6 nm and 8 nm) and deposition geometries (uniform and wedge-deposited) through a combination of magneto-optical and spin-dynamic measurement techniques, including MOKE, VSM, ST-FMR, and FMR. These complementary methods enabled us to obtain a comprehensive understanding of both static and dynamic magnetic properties across different sample configurations.

Initial characterizations using MOKE and VSM provided direct insight into the in-plane magnetic anisotropy of the samples. The results confirmed that the wedge-deposited samples exhibited uniaxial anisotropy aligned with the deposition direction, while the uniform samples displayed nearly isotropic magnetic behavior. Moreover, the degree of anisotropy was found to be stronger in the thicker (8 nm) CoFeB films compared to the thinner (6 nm) ones, consistent across both measurement techniques.

To further probe the dynamic magnetic behavior and quantify parameters such as effective anisotropy fields, damping constants, and demagnetization fields, we performed ST-FMR and FMR measurements. In the ST-FMR frequency scans, the extracted parameters such as the effective demagnetization field ($4\pi M_{eff}$), damping constant (α), $H_{k0}$, and $H_u$ reflected the expected thickness dependence and highlighted the influence



doi:10.6342/NTU202501047

of wedge-induced anisotropy. Notably, the angular dependence study via ST-FMR revealed a clear cos(2θ) modulation in wedge samples, further confirming the presence of a strong uniaxial anisotropy. However, a systematic offset in the fitted anisotropy center ($H_{k0}$) was observed, which we attribute to the shape anisotropy introduced during the lithographic patterning process required for ST-FMR device fabrication.

FMR measurements on unpatterned samples provided an important comparison, offering insights free from patterning-related artifacts. The frequency-dependent Kittel fits and angular-dependent measurements reaffirmed the ST-FMR results, particularly in terms of relative trends in damping and anisotropy strength. The absence of a noticeable offset in the $H_k$ angular dependence from FMR, compared to ST-FMR, further supports the conclusion that patterning contributes to the observed shift in $H_{k0}$ in ST-FMR. Additionally, FMR allowed broader frequency coverage in angular scans, enabling more reliable extraction of parameters like damping and $H_u$ across different angles.

Through cross-validation between ST-FMR and FMR, the extracted parameters—demagnetization fields, damping constants, $H_k$, and $H_u$—showed consistent trends, underscoring the reliability of both measurement techniques. While ST-FMR is advantageous in probing spin-orbit torques and minimizing sample-to-sample variation via device fabrication, it inherently introduces geometric constraints that can affect



doi:10.6342/NTU202501047

certain magnetic parameters. On the other hand, FMR offers a simpler, non-destructive approach that preserves the sample and allows broader angular and frequency exploration.

In summary, this work not only demonstrates the thickness- and geometry-dependent anisotropy in CoFeB films but also emphasizes the importance of combining different characterization techniques to fully capture the static and dynamic magnetic properties. These findings offer valuable guidance for future magnetic device engineering, especially where controlled anisotropy and low damping are critical.



doi:10.6342/NTU202501047

# V. Reference


[1] A. Khvalkovskiy *et al.*, "Basic principles of STT-MRAM cell operation in memory arrays," *J. Phys. D: Appl. Phys.*, vol. 46, no. 7, p. 074001, 2013.

[2] C. Chappert, A. Fert, and F. N. Van Dau, "The emergence of spin electronics in data storage," *Nature materials*, vol. 6, no. 11, pp. 813-823, 2007.

[3] D. D. Tang and C.-F. Pai, *MAGNETIC MEMORY TECHNOLOGY: Spin-transfer-torque Mram and Beyond*. John Wiley & Sons, 2020.

[4] J. Lenz and S. Edelstein, "Magnetic sensors and their applications," *IEEE Sens. J.*, vol. 6, no. 3, pp. 631-649, 2006, doi: 10.1109/jsen.2006.874493.

[5] J. Torrejon *et al.*, "Neuromorphic computing with nanoscale spintronic oscillators," *Nature*, vol. 547, no. 7664, pp. 428-431, 2017.

[6] W. Sucksmith and J. E. Thompson, "The magnetic anisotropy of cobalt," *Proceedings of the Royal Society of London. Series A. Mathematical and Physical Sciences*, vol. 225, no. 1162, pp. 362-375, 1954.

[7] M. Johnson, P. Bloemen, F. Den Broeder, and J. De Vries, "Magnetic anisotropy in metallic multilayers," *Rep. Prog. Phys.*, vol. 59, no. 11, p. 1409, 1996.

[8] J. Cui, T. W. Shield, and R. D. James, "Phase transformation and magnetic anisotropy of an iron–palladium ferromagnetic shape-memory alloy," *Acta Mater.*, vol. 52, no. 1, pp. 35-47, 2004, doi: 10.1016/j.actamat.2003.08.024.

[9] S. Oyarzun, A. Tamion, F. Tournus, V. Dupuis, and M. Hillenkamp, "Size effects in the magnetic anisotropy of embedded cobalt nanoparticles: from shape to surface," *Sci Rep*, vol. 5, p. 14749, Oct 6 2015, doi: 10.1038/srep14749.

[10] D. Sander, "The correlation between mechanical stress and magnetic anisotropy inultrathin films," *Rep. Prog. Phys.*, vol. 62, no. 5, p. 809, 1999.




doi:10.6342/NTU202501047

[11] L. Varga, Z. Gercsi, G. Kovács, A. Kákay, and F. Mazaleyrat, "Stress-induced magnetic anisotropy in nanocrystalline alloys," *J. Magn. Magn. Mater.*, vol. 254, pp. 477-479, 2003.

[12] B. Hofmann and H. Kronmüller, "Stress-induced magnetic anisotropy in nanocrystalline FeCuNbSiB alloy," *J. Magn. Magn. Mater.*, vol. 152, no. 1-2, pp. 91-98, 1996.

[13] W. H. Meiklejohn and C. P. Bean, "New Magnetic Anisotropy," *Phys. Rev.*, vol. 105, no. 3, pp. 904-913, 1957, doi: 10.1103/PhysRev.105.904.

[14] Z. Liang, X.-y. Sun, C.-y. Xu, R.-s. Gao, R.-g. Xu, and L.-c. Qin, "Magnetic anisotropy in Fe-25Cr-12Co-1Si alloy induced by external magnetic field," *Transactions of Nonferrous Metals Society of China*, vol. 17, no. 2, pp. 346-350, 2007.

[15] J. Hu and R. Wu, "Control of the magnetism and magnetic anisotropy of a single-molecule magnet with an electric field," *Phys. Rev. Lett.*, vol. 110, no. 9, p. 097202, Mar 1 2013, doi: 10.1103/PhysRevLett.110.097202.

[16] S. J. Gamble *et al.*, "Electric field induced magnetic anisotropy in a ferromagnet," *Phys. Rev. Lett.*, vol. 102, no. 21, p. 217201, May 29 2009, doi: 10.1103/PhysRevLett.102.217201.

[17] R. Prozorov and V. G. Kogan, "Effective Demagnetizing Factors of Diamagnetic Samples of Various Shapes," *Physical Review Applied*, vol. 10, no. 1, 2018, doi: 10.1103/PhysRevApplied.10.014030.

[18] D. X. Chen, E. Pardo, and A. Sanchez, "Demagnetizing factors for rectangular prisms," *IEEE Trans. Magn.*, vol. 41, no. 6, pp. 2077-2088, 2005, doi: 10.1109/tmag.2005.847634.

[19] S. Piramanayagam, "Perpendicular recording media for hard disk drives," *J. Appl. Phys.*, vol. 102, no. 1, 2007.



doi:10.6342/NTU202501047

[20] B. Tudu and A. Tiwari, "Recent developments in perpendicular magnetic anisotropy thin films for data storage applications," *Vacuum*, vol. 146, pp. 329-341, 2017.

[21] B. Dieny and M. Chshiev, "Perpendicular magnetic anisotropy at transition metal/oxide interfaces and applications," *Rev. Mod. Phys.*, vol. 89, no. 2, 2017, doi: 10.1103/RevModPhys.89.025008.

[22] W. Meiklejohn, "Exchange anisotropy—A review," *J. Appl. Phys.*, vol. 33, no. 3, pp. 1328-1335, 1962.

[23] C. Daboo *et al.*, "Anisotropy and orientational dependence of magnetization reversal processes in epitaxial ferromagnetic thin films," *Phys Rev B Condens Matter*, vol. 51, no. 22, pp. 15964-15973, Jun 1 1995, doi: 10.1103/physrevb.51.15964.

[24] M. Sagawa *et al.*, "Dependence of coercivity on the anisotropy field in the Nd2Fe14B-type sintered magnets," *J. Appl. Phys.*, vol. 61, no. 8, pp. 3559-3561, 1987, doi: 10.1063/1.338725.

[25] K. Bukharia, P. Karmakar, D. Kumar, V. R. Reddy, and A. Gupta, "Evolution of magnetic anisotropy in cobalt film on nanopatterned silicon substrate studied in situ using MOKE," *J. Magn. Magn. Mater.*, vol. 497, 2020, doi: 10.1016/j.jmmm.2019.165934.

[26] M. Igarashi, T. Kambe, K. Yoshida, Y. Hosoe, and Y. Sugita, "A method of measuring anisotropy field of polycrystalline thin-film media," *J. Appl. Phys.*, vol. 85, no. 8, pp. 4720-4722, 1999, doi: 10.1063/1.370459.

[27] A. Barranco, A. Borras, A. R. Gonzalez-Elipe, and A. Palmero, "Perspectives on oblique angle deposition of thin films: From fundamentals to devices," *Prog. Mater Sci.*, vol. 76, pp. 59-153, 2016, doi: 10.1016/j.pmatsci.2015.06.003.

[28] L. Merryweather and A. T. Hindmarch, "Analysis of Magnetization Dynamics in NiFe Thin Films with Growth-Induced Magnetic Anisotropies,"



doi:10.6342/NTU202501047

*Magnetochemistry*, vol. 10, no. 10, 2024, doi: 10.3390/magnetochemistry10100080.

[29] S. Sun Lee, T.-S. Ju, K.-W. Moon, and S. Yang, "Perpendicular magnetic anisotropy tilting for spin–orbit torque-induced field-free switching of magnetization," *J. Magn. Magn. Mater.*, vol. 589, 2024, doi: 10.1016/j.jmmm.2023.171567.

[30] Y.-H. Huang, J.-H. Han, W.-B. Liao, C.-Y. Hu, Y.-T. Liu, and C.-F. Pai, "Tailoring interlayer chiral exchange by azimuthal symmetry engineering," *Nano Lett.*, vol. 24, no. 2, pp. 649-656, 2024.

[31] R. Conley *et al.*, "Wedged multilayer Laue lens," *Rev. Sci. Instrum.*, vol. 79, no. 5, p. 053104, May 2008, doi: 10.1063/1.2924209.

[32] J. S. Cooper, G. Zhang, and P. J. McGinn, "Plasma sputtering system for deposition of thin film combinatorial libraries," *Rev. Sci. Instrum.*, vol. 76, no. 6, 2005.

[33] R. A. Rao, D. Lavric, T. K. Nath, C. B. Eom, L. Wu, and F. Tsui, "Effects of film thickness and lattice mismatch on strain states and magnetic properties of La0.8Ca0.2MnO3 thin films," *J. Appl. Phys.*, vol. 85, no. 8, pp. 4794-4796, 1999, doi: 10.1063/1.370484.

[34] O. Thomas, Q. Shen, P. Schieffer, N. Tournerie, and B. Lepine, "Interplay between anisotropic strain relaxation and uniaxial interface magnetic anisotropy in epitaxial Fe films on (001) GaAs," *Phys. Rev. Lett.*, vol. 90, no. 1, p. 017205, Jan 10 2003, doi: 10.1103/PhysRevLett.90.017205.

[35] T. J. Vink, W. Walrave, J. L. C. Daams, A. G. Dirks, M. A. J. Somers, and K. J. A. van den Aker, "Stress, strain, and microstructure in thin tungsten films deposited by dc magnetron sputtering," *J. Appl. Phys.*, vol. 74, no. 2, pp. 988-995, 1993, doi: 10.1063/1.354842.



doi:10.6342/NTU202501047

[36] Y. Hoshi, E. Suzuki, and M. Naoe, "Uniaxial magnetic anisotropy of iron thin films deposited by oblique incidence of deposition particles," *J. Appl. Phys.*, vol. 79, no. 8, pp. 4945-4947, 1996, doi: 10.1063/1.361597.

[37] Y. Park, E. E. Fullerton, and S. D. Bader, "Growth-induced uniaxial in-plane magnetic anisotropy for ultrathin Fe deposited on MgO(001) by oblique-incidence molecular beam epitaxy," *Appl. Phys. Lett.*, vol. 66, no. 16, pp. 2140-2142, 1995, doi: 10.1063/1.113929.

[38] C. Kittel, "On the Theory of Ferromagnetic Resonance Absorption," *Phys. Rev.*, vol. 73, no. 2, pp. 155-161, 1948, doi: 10.1103/PhysRev.73.155.

[39] V. Denysenkov and A. M. Grishin, "Broadband ferromagnetic resonance spectrometer," *Rev. Sci. Instrum.*, vol. 74, no. 7, pp. 3400-3405, 2003.

[40] C. Hseih, W. Huang, and J. Lue, "The change from paramagnetic resonance to ferromagnetic resonance for iron nanoparticles made by the sol–gel method," *J. Phys. Chem. Solids*, vol. 63, no. 5, pp. 733-741, 2002.

[41] N. Bloembergen, "On the ferromagnetic resonance in nickel and supermalloy," *Phys. Rev.*, vol. 78, no. 5, p. 572, 1950.

[42] R. L. White and I. H. Solt, "Multiple Ferromagnetic Resonance in Ferrite Spheres," *Phys. Rev.*, vol. 104, no. 1, pp. 56-62, 1956, doi: 10.1103/PhysRev.104.56.

[43] S. S. Kalarickal *et al.*, "Ferromagnetic resonance linewidth in metallic thin films: Comparison of measurement methods," *J. Appl. Phys.*, vol. 99, no. 9, 2006.

[44] I. S. Maksymov and M. Kostylev, "Broadband stripline ferromagnetic resonance spectroscopy of ferromagnetic films, multilayers and nanostructures," *Physica E: Low-dimensional Systems and Nanostructures*, vol. 69, pp. 253-293, 2015, doi: 10.1016/j.physe.2014.12.027.



doi:10.6342/NTU202501047

[45] Y. Ding, T. J. Klemmer, and T. M. Crawford, "A coplanar waveguide permeameter for studying high-frequency properties of soft magnetic materials," *J. Appl. Phys.*, vol. 96, no. 5, pp. 2969-2972, 2004, doi: 10.1063/1.1774242.

[46] M. Bailleul, "Shielding of the electromagnetic field of a coplanar waveguide by a metal film: Implications for broadband ferromagnetic resonance measurements," *Appl. Phys. Lett.,* vol. 103, no. 19, 2013, doi: 10.1063/1.4829367.

[47] C. Bilzer, T. Devolder, P. Crozat, C. Chappert, S. Cardoso, and P. Freitas, "Vector network analyzer ferromagnetic resonance of thin films on coplanar waveguides: Comparison of different evaluation methods," *J. Appl. Phys.*, vol. 101, no. 7, 2007.

[48] W. Chen, J.-M. Beaujour, G. De Loubens, A. Kent, and J. Sun, "Spin-torque driven ferromagnetic resonance of Co⁄Ni synthetic layers in spin valves," *Appl. Phys. Lett.*, vol. 92, no. 1, 2008.

[49] T. Chiba, G. E. W. Bauer, and S. Takahashi, "Current-Induced Spin-Torque Resonance of Magnetic Insulators," *Physical Review Applied,* vol. 2, no. 3, 2014, doi: 10.1103/PhysRevApplied.2.034003.

[50] Y. Wang, R. Ramaswamy, and H. Yang, "FMR-related phenomena in spintronic devices," *J. Phys. D: Appl. Phys.*, vol. 51, no. 27, 2018, doi: 10.1088/1361-6463/aac7b5.

[51] D. C. Ralph and M. D. Stiles, "Spin transfer torques," *J. Magn. Magn. Mater.,* vol. 320, no. 7, pp. 1190-1216, 2008, doi: 10.1016/j.jmmm.2007.12.019.

[52] Q. Shao *et al.*, "Roadmap of Spin–Orbit Torques," *IEEE Trans. Magn.*, vol. 57, no. 7, pp. 1-39, 2021, doi: 10.1109/tmag.2021.3078583.

[53] P. Gambardella and I. M. Miron, "Current-induced spin-orbit torques," *Philos Trans A Math Phys Eng Sci,* vol. 369, no. 1948, pp. 3175-97, Aug 13 2011, doi: 10.1098/rsta.2010.0336.



doi:10.6342/NTU202501047

[54] C.-J. Zhao, L. Ding, J.-S. HuangFu, J.-Y. Zhang, and G.-H. Yu, "Research progress in anisotropic magnetoresistance," *Rare Metals,* vol. 32, no. 3, pp. 213-224, 2013, doi: 10.1007/s12598-013-0090-5.

[55] A. W. Rushforth *et al.*, "Anisotropic magnetoresistance components in (Ga,Mn)As," *Phys. Rev. Lett.,* vol. 99, no. 14, p. 147207, Oct 5 2007, doi: 10.1103/PhysRevLett.99.147207.

[56] H. Nakayama *et al.*, "Spin Hall magnetoresistance induced by a nonequilibrium proximity effect," *Phys. Rev. Lett.,* vol. 110, no. 20, p. 206601, May 17 2013, doi: 10.1103/PhysRevLett.110.206601.

[57] Y.-T. Chen *et al.*, "Theory of spin Hall magnetoresistance," *Physical Review B,* vol. 87, no. 14, 2013, doi: 10.1103/PhysRevB.87.144411.

[58] M. N. Baibich *et al.*, "Giant magnetoresistance of (001)Fe/(001)Cr magnetic superlattices," *Phys. Rev. Lett.,* vol. 61, no. 21, pp. 2472-2475, Nov 21 1988, doi: 10.1103/PhysRevLett.61.2472.

[59] J. Q. Xiao, J. S. Jiang, and C. L. Chien, "Giant magnetoresistance in nonmultilayer magnetic systems," *Phys. Rev. Lett.,* vol. 68, no. 25, pp. 3749-3752, Jun 22 1992, doi: 10.1103/PhysRevLett.68.3749.

[60] S.-K. Kim, "Micromagnetic computer simulations of spin waves in nanometre-scale patterned magnetic elements," *J. Phys. D: Appl. Phys.,* vol. 43, no. 26, 2010, doi: 10.1088/0022-3727/43/26/264004.

[61] J. Hirsch, "Spin hall effect," *Phys. Rev. Lett.,* vol. 83, no. 9, p. 1834, 1999.

[62] J. Sinova, S. O. Valenzuela, J. Wunderlich, C. H. Back, and T. Jungwirth, "Spin Hall effects," *Rev. Mod. Phys.,* vol. 87, no. 4, pp. 1213-1260, 2015, doi: 10.1103/RevModPhys.87.1213.

[63] R. James, Y. Pilloux, and H. Hegde, "Reactive ion beam etching of piezoelectric ScAlN for bulk acoustic wave device applications," in *Journal of Physics: Conference Series*, 2019, vol. 1407, no. 1: IOP Publishing, p. 012083.



doi:10.6342/NTU202501047

[64] A. Barman, T. Kimura, Y. Otani, Y. Fukuma, K. Akahane, and S. Meguro, "Benchtop time-resolved magneto-optical Kerr magnetometer," *Rev. Sci. Instrum.*, vol. 79, no. 12, p. 123905, Dec 2008, doi: 10.1063/1.3053353.

[65] S. Foner, "The vibrating sample magnetometer: Experiences of a volunteer (invited)," *J. Appl. Phys.*, vol. 79, no. 8, pp. 4740-4745, 1996, doi: 10.1063/1.361657.

[66] S. Jen *et al.*, "Magnetic and electrical properties of amorphous CoFeB films," *J. Appl. Phys.*, vol. 99, no. 5, 2006.

[67] B. Liu and J. Ding, "Strain-induced high coercivity in CoFe2O4 powders," *Appl. Phys. Lett.*, vol. 88, no. 4, 2006.

[68] Y.-P. Zhao, R. Gamache, G.-C. Wang, T.-M. Lu, G. Palasantzas, and J. T. M. De Hosson, "Effect of surface roughness on magnetic domain wall thickness, domain size, and coercivity," *J. Appl. Phys.*, vol. 89, no. 2, pp. 1325-1330, 2001.

[69] O. Gutfleisch *et al.*, "Evolution of magnetic domain structures and coercivity in high-performance SmCo 2:17-type permanent magnets," *Acta Mater.*, vol. 54, no. 4, pp. 997-1008, 2006, doi: 10.1016/j.actamat.2005.10.026.

[70] T. Su, Z. Rao, S. Berman, D. Depla, and E. Chason, "Analysis of stress in sputter-deposited films using a kinetic model for Cu, Ni, Co, Cr, Mo, W," *Appl. Surf. Sci.*, vol. 613, 2023, doi: 10.1016/j.apsusc.2022.156000.

[71] F. Hubenthal, T. Stobiecki, K. Thoma, and K. Röll, "Anisotropic residual stresses in sputtered TiN films prepared by linear periodic motion," *Surf. Coat. Technol.*, vol. 201, no. 6, pp. 3399-3405, 2006, doi: 10.1016/j.surfcoat.2006.07.213.

[72] H. Takagi, S. Tsunashima, S. Uchiyama, and T. Fujii, "Stress induced anisotropy in amorphous Gd-Fe and Tb-Fe sputtered films," *J. Appl. Phys.*, vol. 50, no. B3, pp. 1642-1644, 1979, doi: 10.1063/1.327223.



doi:10.6342/NTU202501047

[73] N. Chowdhury and S. Bedanta, "Controlling the anisotropy and domain structure with oblique deposition and substrate rotation," *AIP Advances,* vol. 4, no. 2, 2014, doi: 10.1063/1.4865248.

[74] S. Mallik, S. Mallick, and S. Bedanta, "Effect of the growth conditions on the anisotropy, domain structures and the relaxation in Co thin films," *J. Magn. Magn. Mater.,* vol. 428, pp. 50-58, 2017, doi: 10.1016/j.jmmm.2016.11.132.

[75] A. N. Bogdanov and U. K. Rossler, "Chiral symmetry breaking in magnetic thin films and multilayers," *Phys. Rev. Lett.,* vol. 87, no. 3, p. 037203, Jul 16 2001, doi: 10.1103/PhysRevLett.87.037203.

[76] Y. V. Goryunov *et al.,* "Magnetic anisotropies of sputtered Fe films on MgO substrates," *Phys Rev B Condens Matter,* vol. 52, no. 18, pp. 13450-13458, Nov 1 1995, doi: 10.1103/physrevb.52.13450.

[77] E. Liu *et al.,* "Texture induced magnetic anisotropy in Fe3O4 films," *Appl. Phys. Lett.,* vol. 107, no. 17, 2015, doi: 10.1063/1.4934744.

[78] C. Tannous and J. Gieraltowski, "The Stoner–Wohlfarth model of ferromagnetism," *European Journal of Physics,* vol. 29, no. 3, pp. 475-487, 2008, doi: 10.1088/0143-0807/29/3/008.

[79] A. Thiaville, "Coherent rotation of magnetization in three dimensions: A geometrical approach," *Physical Review B,* vol. 61, no. 18, p. 12221, 2000.

[80] D. Givord, P. Tenaud, and T. Viadieu, "Angular dependence of coercivity in sintered magnets," *J. Magn. Magn. Mater.,* vol. 72, no. 3, pp. 247-252, 1988.

[81] F. Yang, C. Chien, E. Ferrari, X. Li, G. Xiao, and A. Gupta, "Uniaxial anisotropy and switching behavior in epitaxial CrO~ 2 films," *Appl. Phys. Lett.,* vol. 77, no. 2, pp. 286-288, 2000.

[82] Y. H. Shin, I. Grinberg, I. W. Chen, and A. M. Rappe, "Nucleation and growth mechanism of ferroelectric domain-wall motion," *Nature,* vol. 449, no. 7164, pp. 881-4, Oct 18 2007, doi: 10.1038/nature06165.



doi:10.6342/NTU202501047

[83] C. He *et al.*, "Spin-Torque Ferromagnetic Resonance in W/Co−Fe−B/W/Co−Fe−B/MgO Stacks," *Physical Review Applied,* vol. 10, no. 3, 2018, doi: 10.1103/PhysRevApplied.10.034067.

[84] C. He *et al.*, "Spin-torque ferromagnetic resonance measurements utilizing spin Hall magnetoresistance in W/Co40Fe40B20/MgO structures," *Appl. Phys. Lett.*, vol. 109, no. 20, 2016, doi: 10.1063/1.4967843.

[85] S. Zohar and W. Bailey, "Interface-related damping in polycrystalline Ni81Fe19/Cu/Co93Zr7 trilayers," *J. Appl. Phys.*, vol. 105, no. 7, 2009.

[86] M. Caminale *et al.*, "Spin pumping damping and magnetic proximity effect in Pd and Pt spin-sink layers," *Physical Review B,* vol. 94, no. 1, 2016, doi: 10.1103/PhysRevB.94.014414.

[87] V. Sharma, R. K. Ghosh, and B. K. Kuanr, "Influence of ferromagnetic layer thickness on the Gilbert damping and magnetocrystalline anisotropy in PLD grown epitaxial Co2FeSi Heusler alloy thin films," *Results in Surfaces and Interfaces,* vol. 6, 2022, doi: 10.1016/j.rsurfi.2022.100052.

[88] N. Fujita, N. Inaba, F. Kirino, S. Igarashi, K. Koike, and H. Kato, "Damping constant of Co/Pt multilayer thin-film media," *J. Magn. Magn. Mater.*, vol. 320, no. 22, pp. 3019-3022, 2008, doi: 10.1016/j.jmmm.2008.08.012.

[89] K. Lenz, H. Wende, W. Kuch, K. Baberschke, K. Nagy, and A. Jánossy, "Two-magnon scattering and viscous Gilbert damping in ultrathin ferromagnets," *Physical Review B,* vol. 73, no. 14, 2006, doi: 10.1103/PhysRevB.73.144424.

[90] K. Zakeri *et al.*, "Spin dynamics in ferromagnets: Gilbert damping and two-magnon scattering," *Physical Review B,* vol. 76, no. 10, 2007, doi: 10.1103/PhysRevB.76.104416.

[91] Y. Li *et al.*, "Drag effect induced large anisotropic damping behavior in magnetic thin films with strong magnetic anisotropy," *J. Phys.: Condens. Matter,* vol. 33, no. 17, p. 175801, 2021.



doi:10.6342/NTU202501047

[92] Y. Kasatani and Y. Nozaki, "Crystallographic anisotropy of the intrinsic Gilbert damping for single-crystalline Fe film," *Journal of the Magnetics Society of Japan*, vol. 39, no. 6, pp. 221-226, 2015.

[93] A. Conca, S. Keller, M. R. Schweizer, E. T. Papaioannou, and B. Hillebrands, "Separation of the two-magnon scattering contribution to damping for the determination of the spin mixing conductance," *Physical Review B*, vol. 98, no. 21, p. 214439, 2018.



doi:10.6342/NTU202501047

# VI. Supplementary

## 6-1 Raw data

### 6-1.1 Laser-MOKE

The raw data obtained from Laser-MOKE measurements for all samples are shown in Figures S1 to S4. These plots display the hysteresis loops measured under different magnetic field directions, which were used to investigate the angular dependence of the magnetization behavior.



doi:10.6342/NTU202501047

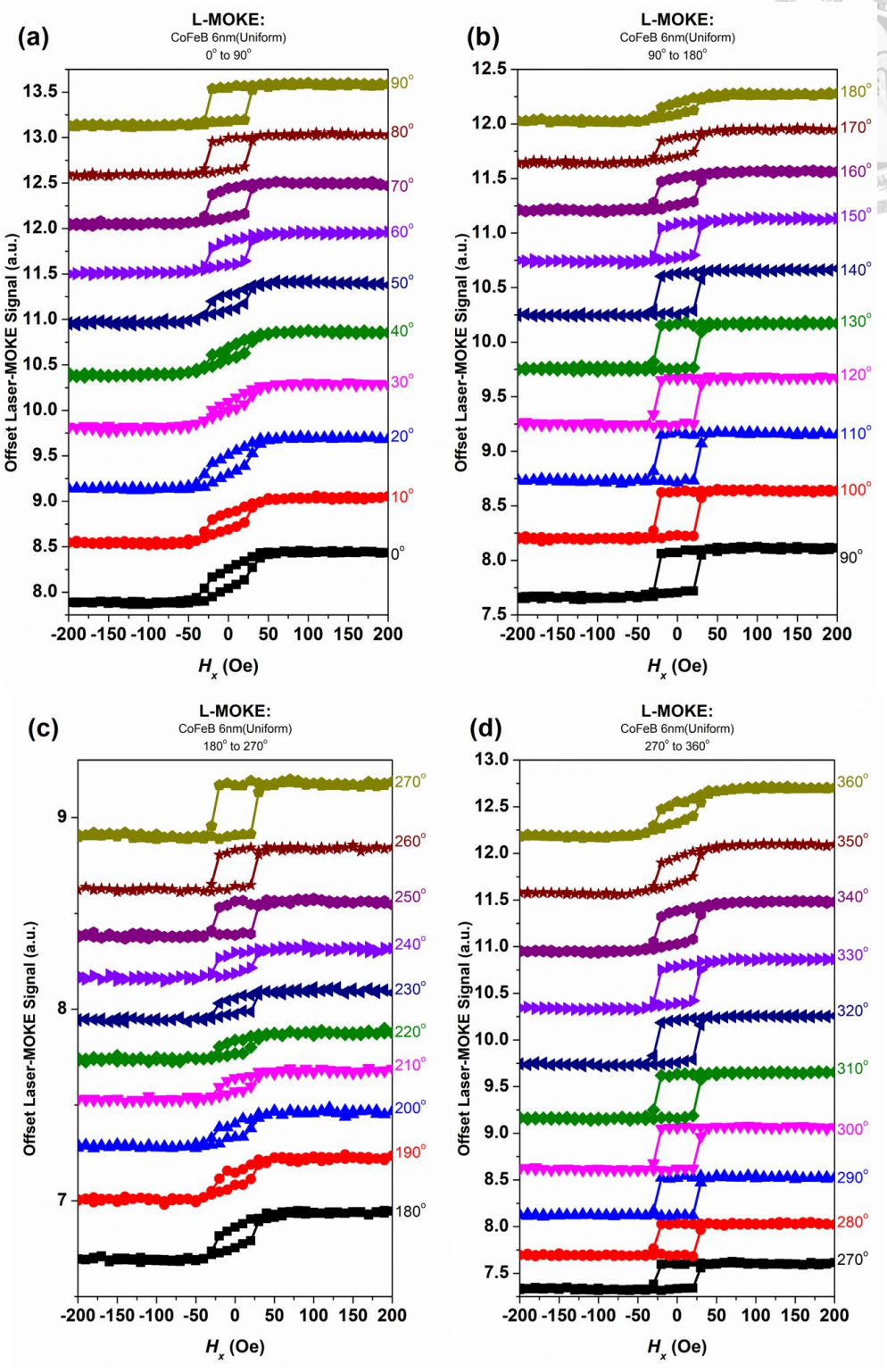


**Figure S. 1** MOKE hysteresis loops of the CoFeB 6nm(Uniform) sample, separated by magnetic field sweep angles: (a) 0˚ – 90˚, (b) 90˚ – 180˚, (c) 180˚ – 270˚, and (d) 270˚ – 360˚



doi:10.6342/NTU202501047

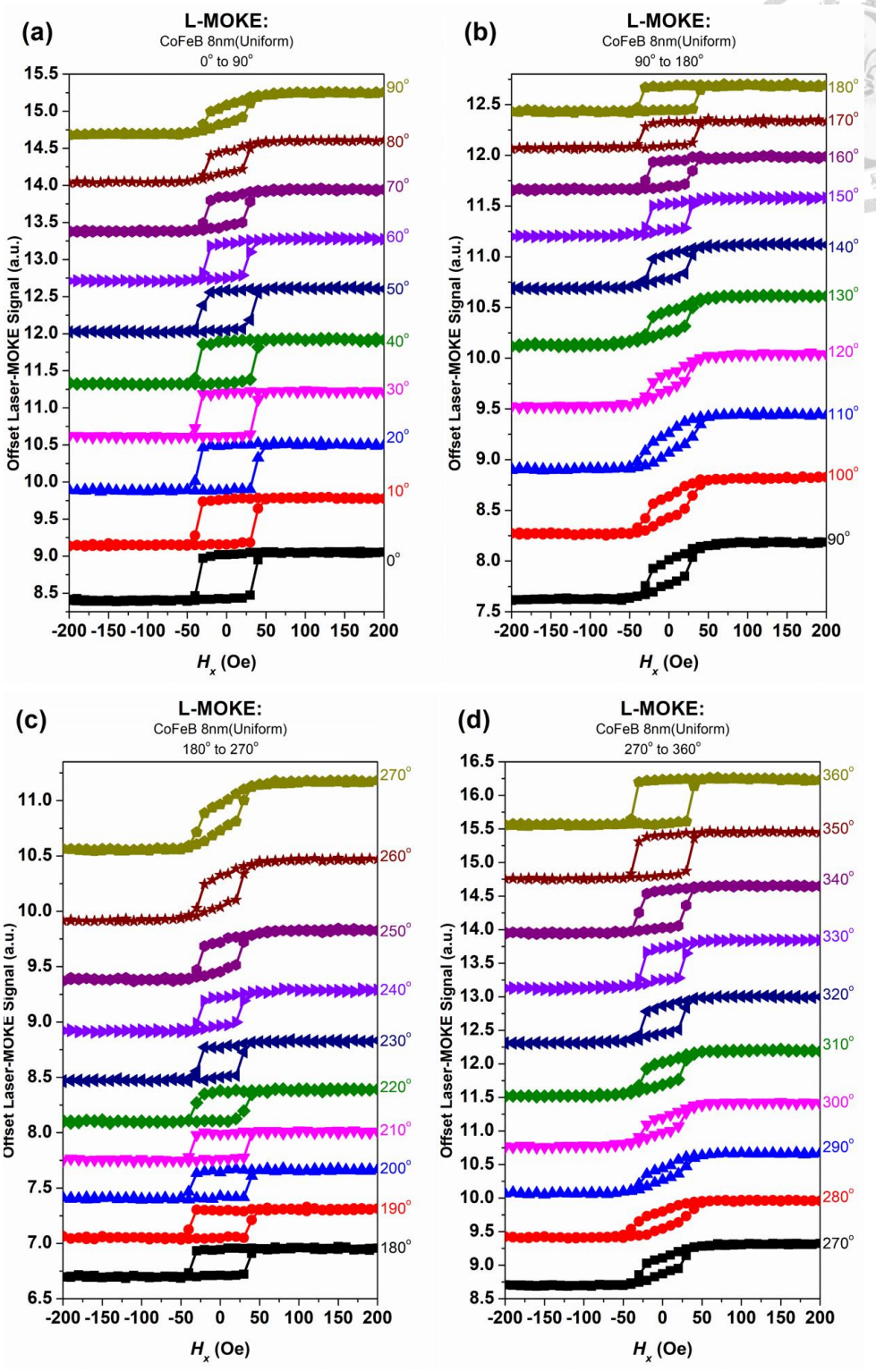


**Figure S. 2** MOKE hysteresis loops of the CoFeB 8nm(Uniform) sample, separated by magnetic field sweep angles: (a) 0°–90°, (b) 90°–180°, (c) 180°–270°, and (d) 270°–360°



doi:10.6342/NTU202501047

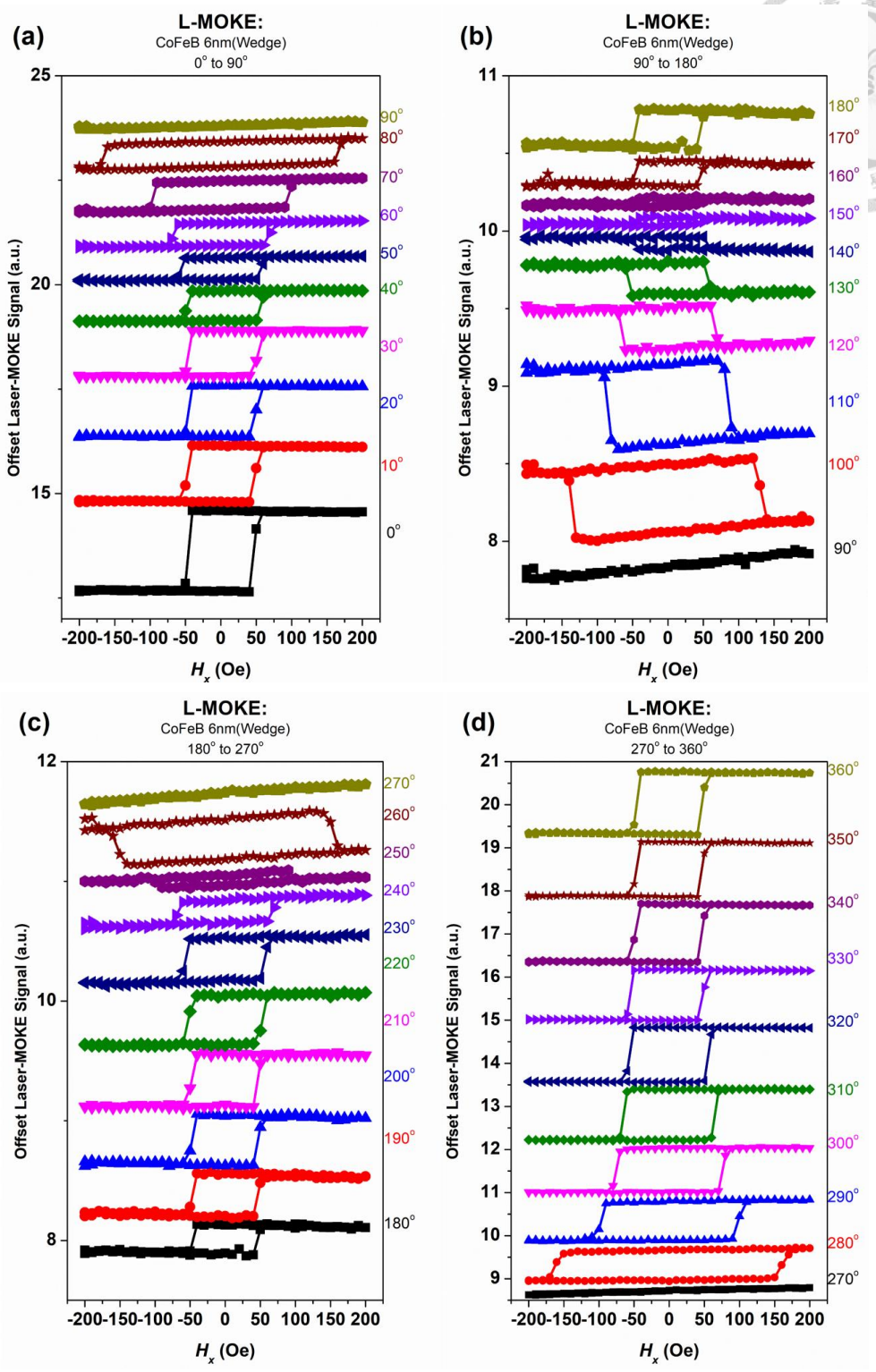


**Figure S. 3** MOKE hysteresis loops of the CoFeB 6nm(Wedge) sample, separated by magnetic field sweep angles: (a) 0°–90°, (b) 90°–180°, (c) 180°–270°, and (d) 270°–360°



doi:10.6342/NTU202501047

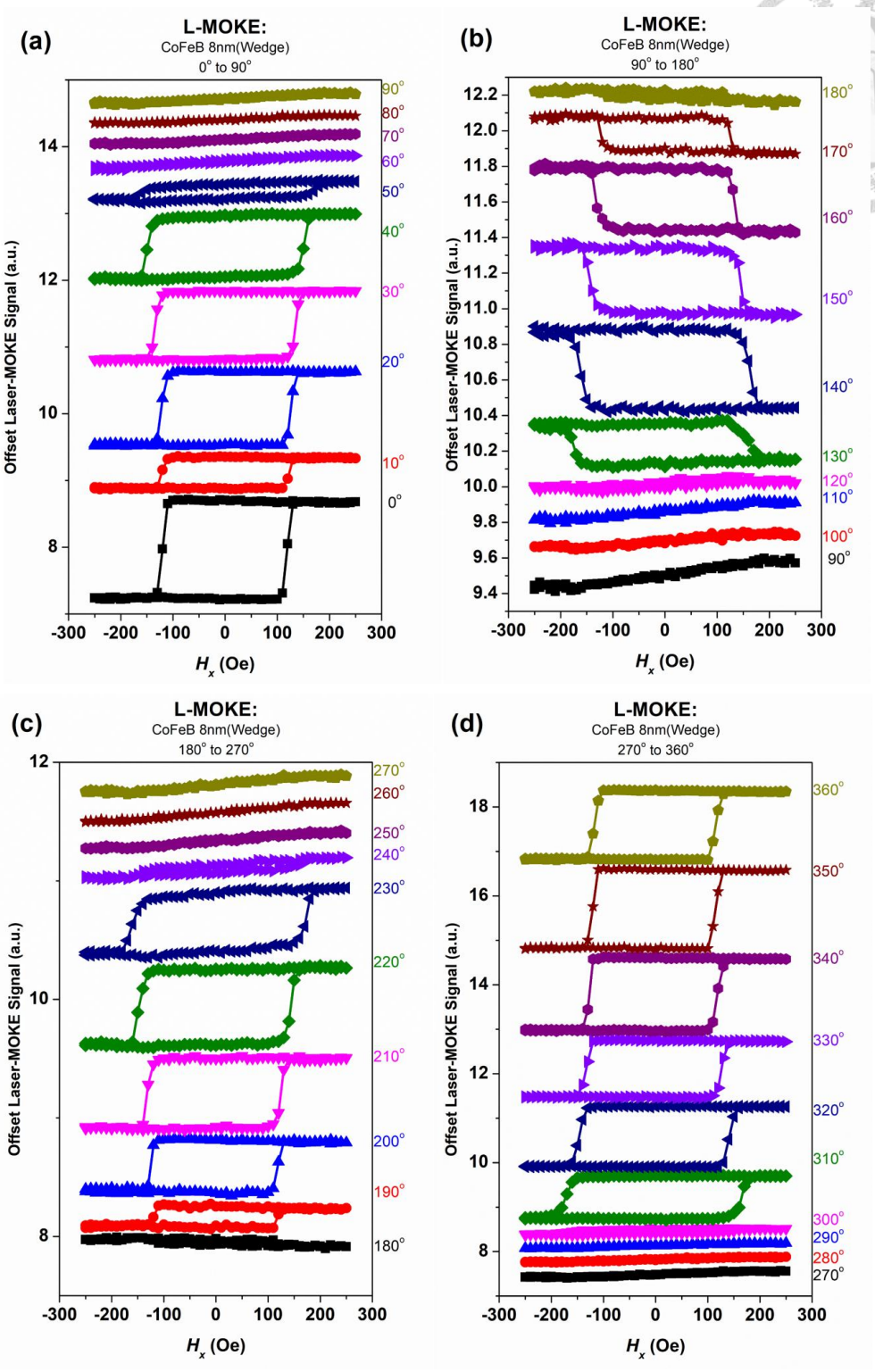


**Figure S. 4** MOKE hysteresis loops of the CoFeB 8nm(Wedge) sample, separated by magnetic field sweep angles: (a) 0˚ – 90˚, (b) 90˚ – 180˚, (c) 180˚ – 270˚, and (d) 270˚ – 360˚



doi:10.6342/NTU202501047

# 6-1.2 ST-FMR

The raw data obtained from ST-FMR measurements, including both uniform and wedged, are presented in Figures S5 to S8.

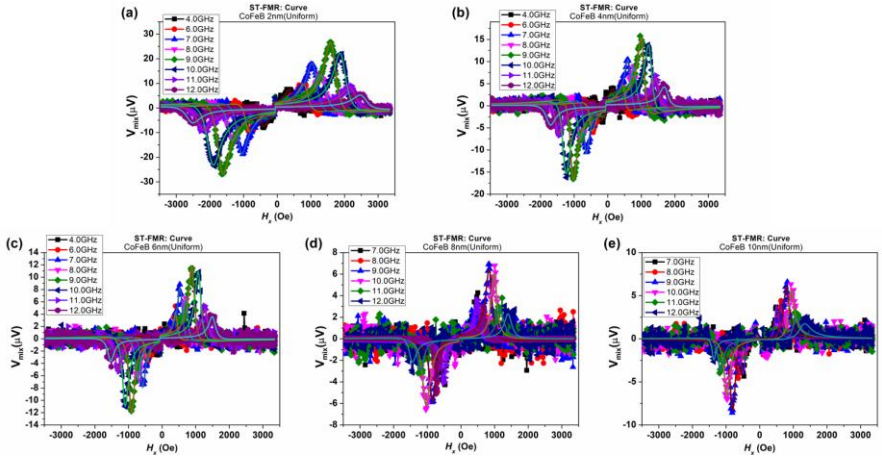


**Figure S. 5** ST-FMR curves of CoFeB (Uniform) samples with different ferromagnetic layer thicknesses:

(a) 2 nm, (b) 4 nm, (c) 6 nm, (d) 8 nm, and (e) 10 nm.

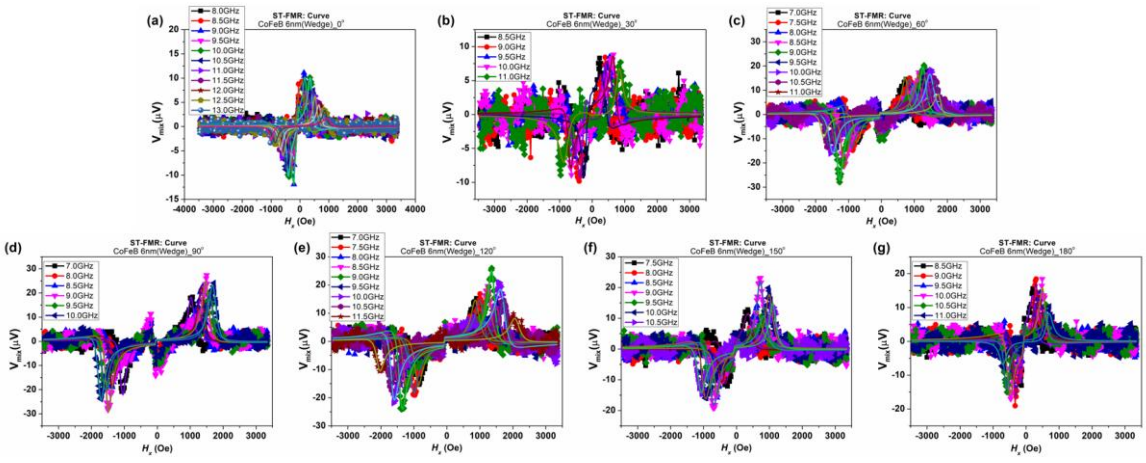


**Figure S. 6** ST-FMR curves of CoFeB 6nm(Wedge) sample with different wedge deposition angle :

(a) 0°, (b)30°, (c) 60°, (d) 90°,(e) 120°.(f) 150°,(g) 180°



doi:10.6342/NTU202501047

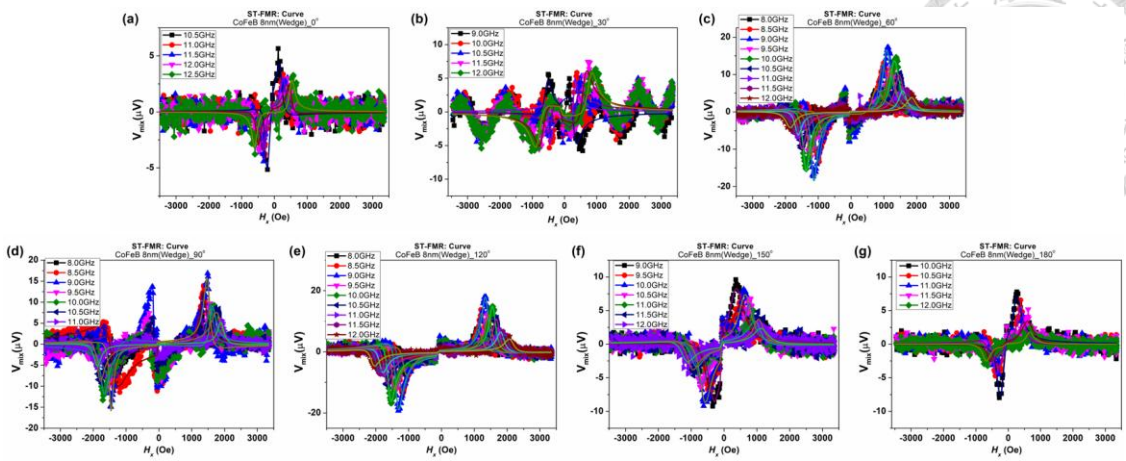


Figure S. 7 ST-FMR curves of CoFeB 8nm(Wedge) sample with different wedge deposition angle :

(a) 0°, (b)30°, (c) 60°, (d) 90°,(e) 120°.(f) 150°,(g) 180°

# 6-1.3 FMR

The raw data from FMR measurements, covering both uniform and wedged, are shown in Figures S9 to S12.

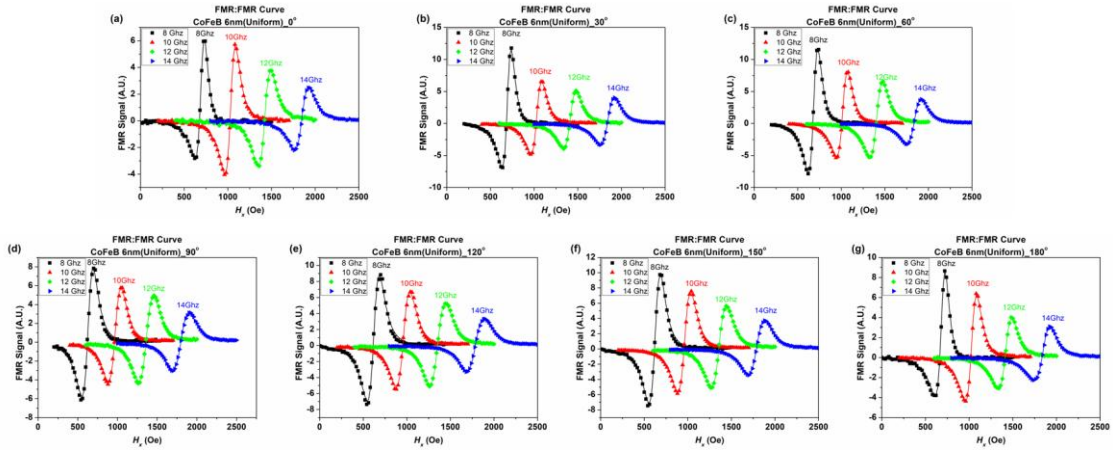


**Figure S. 8** FMR curves of CoFeB 6nm(Uniform) sample with different field angle :

(a) 0°, (b)30°, (c) 60°, (d) 90°,(e) 120°.(f) 150°,(g) 180°



doi:10.6342/NTU202501047

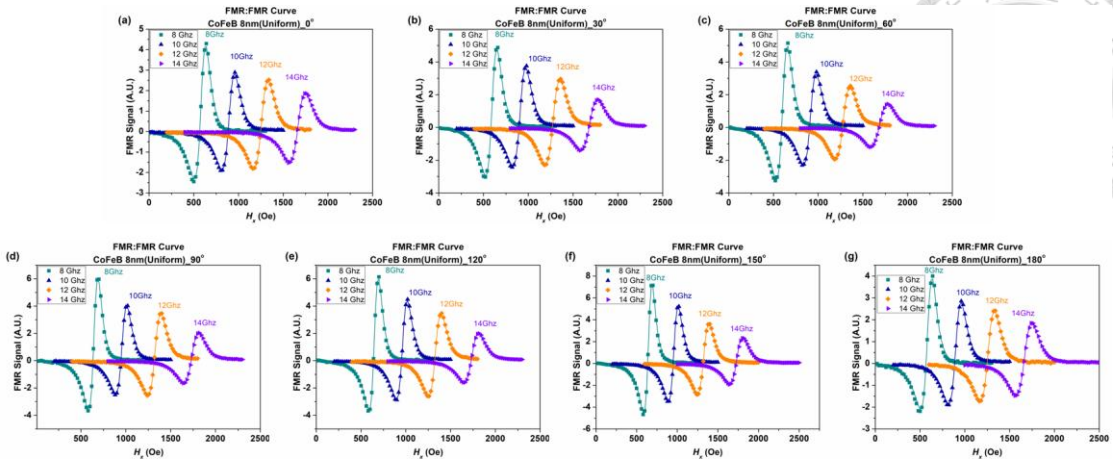


**Figure S. 9** FMR curves of CoFeB 6nm(Uniform) sample with different field angle :

(a) 0°, (b)30°, (c) 60°, (d) 90°,(e) 120°.(f) 150°,(g) 180°

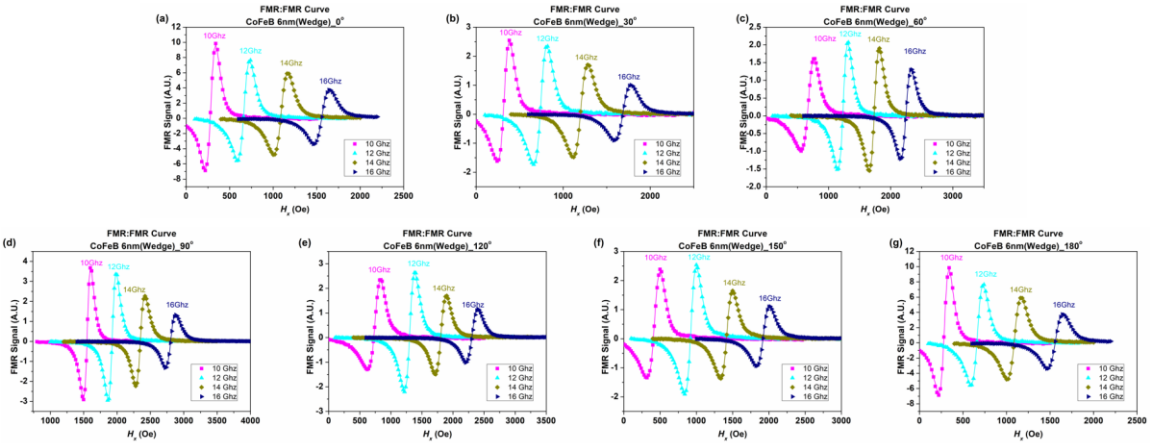


**Figure S. 10** FMR curves of CoFeB 6nm(Wedge) w/ wedge angle 0°sample with different field angle :

(a) 0°, (b)30°, (c) 60°, (d) 90°,(e) 120°.(f) 150°,(g) 180°



doi:10.6342/NTU202501047

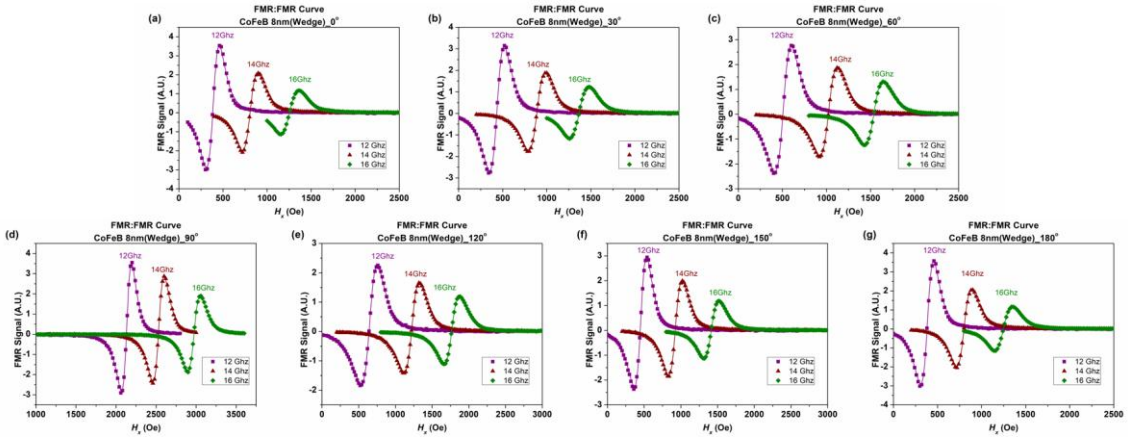


**Figure S. 11** FMR curves of CoFeB 8nm(Wedge) w/ wedge angle 0°sample with different field angle :

(a) 0°, (b)30°, (c) 60°, (d) 90°,(e) 120°.(f) 150°,(g) 180°



doi:10.6342/NTU202501047